



# The relationship between induced three-dimensional vortical structures in the wake and the drag of a profiled blunt trailing edge body

Ross Cruikshank<sup>1</sup> , Satoshi Baba<sup>1</sup> and Philippe Lavoie<sup>1</sup> 

<sup>1</sup>University of Toronto Institute for Aerospace Studies, 4925 Dufferin Street, Toronto, ON M3H 5T6, Canada

**Corresponding author:** Philippe Lavoie, [phil.lavoie@utoronto.ca](mailto:phil.lavoie@utoronto.ca)

(Received 14 January 2024; revised 10 November 2024; accepted 28 December 2024)

Three-dimensional wake forcing is applied to a profiled blunt trailing edge body from synthetic jet arrays distributed symmetrically on both sides of the body. The effect on the wake is experimentally studied at Reynolds numbers based on body thickness,  $d$ , of  $2500 \leq Re_d = u_\infty d / \nu \leq 5000$  in the turbulent wake regime. The exits of the synthetic jets are rectangular slots and are oriented spanwise to the cross-flow with a uniform spacing of  $2.4d$ . The forcing causes spanwise variations in the separated shear layers, leading to the von Kármán vortices tilting and forming coherent streamwise vortex loops. This reorientation of the wake vorticity is associated with the attenuation of the vortex street and drag reduction, consistent with previous studies of spanwise perturbations to wakes. The effect of forcing amplitude on the drag and wake structure is examined. It is found that the mean shedding frequency is constant across the span in all cases, indicating that the forced wake has a periodic organised structure. The greatest drag reduction of approximately 25% is achieved when the vortical structures emitted by the jets penetrate up the edges of the boundary layers of the body, which occurs at velocity ratios (defined from the mean jet exit velocity during expulsion) of about 3 when  $Re_d = 2500$  and about 2 when  $Re_d = 5000$ . This study presents evidence that the forcing effectiveness is maximised when the vortex street is most tilted into the streamwise direction.

**Key words:** drag reduction, vortex shedding, jets

## 1. Introduction

Three-dimensional, or spanwise-varying, perturbations to separated shear layers are one type of control strategy that can break up and weaken the regular vortex street of a bluff body. Early research into this strategy focused on geometric spanwise variations. Tanner (1972) investigated segmented cutouts in the trailing edge of a blunt trailing edge (BTE) airfoil of thickness,  $d$ , at  $Re_d = u_\infty d / \nu \approx 50\,000$ , and measured increasing base pressure levels as the depth of the cutouts increased, up to a maximum base pressure recovery of 64%. Gai & Sharma (1981) investigated a range of different cutout geometries to try and optimise their shape and found that an ‘M’ shape was most effective for drag reduction. With a schlieren technique, Rodriguez (1991) drew attention to the presence of streamwise vortices in the wake of BTE-profiled bodies with different trailing-edge cutouts and hypothesised that their relative effectiveness was related to these induced streamwise vortices.

Wavy surfaces are another way to apply spanwise perturbations to the wake. Ahmed & Bays-Muchmore (1992) and later Ahmed, Khan & Bays-Muchmore (1993) investigated the effect of cylinder waviness in the range of  $0.8d \leq \lambda_z \leq 2.4d$ , where  $\lambda_z$  is the spanwise wavelength. Ahmed *et al.* (1993) examined the separation lines on wavy cylinders and associated the spanwise variations in the width of the wake to the local points of separation. In particular, they found that the wake width and velocity deficit were greater downstream of the cylinder saddles (minimum  $d$ ) than the nodes (maximum  $d$ ). Lam *et al.* (2004) examined the velocity power spectra at different positions along the span for wavy cylinders in the range of  $1.5d \leq \lambda_z \leq 2.3d$  and found that spanwise waviness significantly reduced intensity of the vortex shedding. Notably, the mean frequency of the shedding did not change along the span and, in fact, was almost the same as that for a plain cylinder. The flow structures in the wake of a wavy cylinder with  $\lambda_z = 2d$  at  $Re_d = 3000$  were measured for the first time using particle image velocimetry (PIV) by Zhang & Lee (2005). They identified well-organised streamwise vortices that they related to the suppression of vortex shedding as well as the spanwise wake width variations that were originally characterised by Ahmed *et al.* (1993). Using large-eddy simulations, Lam & Lin (2008) identified that in the range  $1.1d < \lambda_z < 3.3d$  at  $Re_d = 3000$ , the optimal wavelength for drag reduction was  $\lambda_z = 1.9d$ , in line with the experiments of Lee & Nguyen (2007). Lam & Lin (2008) also emphasised that there was only a single mean shedding frequency along the span for all the  $\lambda_z$  that they investigated. Lam & Lin (2009) performed direct numerical simulations focused at  $Re_d = 100$  in order to investigate the optimal  $\lambda_z$  for a wavy cylinder over a wider range of  $1d \leq \lambda_z \leq 10d$ . They identified a local minimum in the drag at  $\lambda_z \approx 2d$ , but also found different flow regimes for  $\lambda_z > 5d$  wherein the wake width shrunk at the saddles (minimum  $d$ ) relative to the nodes (maximum  $d$ ) and the drag was lower than that at  $\lambda_z \approx 2d$ .

Tombazis & Bearman (1997) studied wavy trailing edges on BTE-profiled bodies and found that increasing the wave steepness led to progressively higher base pressure levels up to a maximum recovery of 34% at  $Re_d = 40\,000$ . For  $3.5d \leq \lambda_z \leq 5.6d$ , they noted two shedding frequencies in the wake, with the higher frequency being most evident at the valley positions along the span where the shear layer velocity increased. Tombazis & Bearman (1997) concluded that the mechanism of control was related to the attenuation of the vortex shedding due to the generation of regular vortex dislocations at the positions along the span aligned with the peaks of the wavy trailing edge.

Darekar & Sherwin (2001) performed direct numerical simulations on wavy square prisms to study the effect of the perturbation wavelength on the flow structures and aerodynamic forces. They focused on  $Re_d = 100$  and observed the tilting of spanwise

vorticity into streamwise components and associated this with the weakening of the vortex shedding. The flow field was categorised by Darekar & Sherwin (2001) into different regimes depending on the amplitude and wavelength of the waviness in a fashion similar to that of Lam & Lin (2009) for a wavy cylinder. A critical  $\lambda_z = 5.6d$  was pinpointed by Darekar & Sherwin (2001), below which there was a single shedding frequency, and above which there were two. Cai, Chng & Tsai (2008) employed direct numerical simulations at  $Re_d = 2500$  to investigate the effect of  $\lambda_z$  on the flow structures and drag of a BTE-profiled body. For these types of bodies, Cai *et al.* (2008) found that the streamwise velocity at the trailing edge was greater at the valleys compared with the peaks, causing spanwise flow towards the valley regions and retarding the vortex street at the peak regions. Consistent with the results of Darekar & Sherwin (2001), the  $\lambda_z < 5d$  cases of Cai *et al.* (2008) exhibited only a single shedding frequency, which they termed the spanwise-regular mode. In contrast, the  $\lambda_z > 5d$  cases were termed spanwise-irregular because they had multiple shedding frequencies. They identified that the boundary between these two regimes at  $\lambda_z = 5d$  provided the best drag reduction of 30 % compared with a plain trailing edge.

Park *et al.* (2006) attempted to simplify the spanwise perturbations using small spanwise-separated tabs along the trailing edge of a BTE-profiled body. Similar to the various studies investigating wavy trailing edges, Park *et al.* (2006) observed that the tabs caused spanwise variations in the mean wake velocity field and broke up the vortex street. Additionally, they found that the optimal spacing of the tabs for drag reduction ranged from about  $1.5d$  to  $2.5d$ . For the optimal tab height of about  $0.1d$  at  $Re_d = 40\,000$ , Park *et al.* (2006) reported a base pressure recovery of over 30 %.

The success of the various passive three-dimensional wake control methods motivates the application of active control in order to open up more possible methodologies than are available from geometric changes. Kim *et al.* (2004) were some of the first to formally investigate active three-dimensional wake control, termed distributed forcing. They applied a steady blowing and suction with a spanwise sinusoidally varying velocity profile to both sides of a BTE-profiled body near its trailing edges at  $\lambda_z = 4d$  and realised 36 % and 18 % base pressure recoveries at  $Re_d = 20\,000$  and  $40\,000$ , respectively. Kim & Choi (2005) pursued this strategy using numerical means to examine the effect of the forcing wavelength. When the wake was turbulent at  $Re_d = 3900$ , the mean shedding frequency was constant along the span and forcing caused phase differences in the vortex shedding along the span when  $\lambda_z < 5d$ . In contrast, the shedding frequency varied over the span when  $\lambda_z > 5d$  and vortex dislocations developed as a result (Kim & Choi 2005).

Distributed forcing of a BTE-profiled body with a discrete number of actuators along the span was investigated by Naghib-Lahouti & Hangan (2010) with circular injection ports upstream of the trailing edges and later by Naghib-Lahouti, Hangan & Lavoie (2015) with plasma actuators. The injection ports of Naghib-Lahouti & Hangan (2010) were spaced apart by  $2.1d$  and the plasma actuators of Naghib-Lahouti *et al.* (2015) were spaced  $2.4d$  apart, which was chosen to approximately match the wavelength of a secondary instability structure observed by Naghib-Lahouti, Lavoie & Hangan (2014), referred to as the mode  $B'$ . They argued that by exciting the mode  $B'$ , the vortex street could be maximally disorganized and this would help optimise the forcing effectiveness. Naghib-Lahouti & Hangan (2010) found that forcing at  $Re_d = 400$  was successful in attenuating the unsteady aerodynamic forces, but the effectiveness diminished significantly at  $Re_d = 1000$ , which they attributed to temporal variations in the mode  $B'$  structure. However, Naghib-Lahouti *et al.* (2015) reported that plasma-actuator-distributed forcing caused spanwise variations in the shedding frequency and they achieved a 40 % recovery in the base pressure at  $Re_d = 3000$ . Bhattacharya & Gregory (2015) investigated the effect of the forcing amplitude for a

spanwise array of plasma actuators distributed along on a cylinder at  $Re_d = 4700$ . Similar to Naghib-Lahouti *et al.* (2015), the spacing of the actuators was selected by Bhattacharya & Gregory (2015) to align with the wavelength of a natural secondary wake instability, except they used the mode A and so set  $\lambda_z = 4d$ . Bhattacharya & Gregory (2015) found that the spanwise coherence of the vortex street was reduced with low-power forcing. For high-amplitude forcing, the vortex shedding was significantly attenuated because its supply of circulation was largely cut off. The effect of forcing wavelength over  $1d \leq \lambda_z \leq 6d$  for a cylinder at  $Re_d = 4700$  outfitted with distributed plasma actuators was investigated by Bhattacharya & Gregory (2018). They found that the optimal wavelength range for drag reduction was  $3d \leq \lambda_z \leq 5d$  and related it to measurements of streamwise vortices in the wake. Interestingly, phase-averaging of their vorticity plots to the vortex shedding cycle revealed that the symmetry of their streamwise vortices did not match the mode A secondary instability. They suggested that the optimal  $\lambda_z$  for their forcing strategy was a function of the balance between having a large spanwise impact of the forcing, which increases with shorter  $\lambda_z$ , and generating large vortex dislocations, which increases with longer  $\lambda_z$ .

In summary, previous research involving different types of spanwise perturbations has shown many common threads regarding the mechanism of control, namely the development of streamwise vortices in the wake and the occurrence of vortex dislocations. Some studies, such as Dobre, Hangan & Vickery (2006), Naghib-Lahouti *et al.* (2015) and Bhattacharya & Gregory (2015), have proposed that the control mechanism is related to matching the forcing to the dominant natural secondary instabilities of the wake. This study builds upon the previous research of Naghib-Lahouti *et al.* (2015), so a similar BTE-profiled body geometry is adopted and the spacing of the actuators is pre-selected to match the  $\lambda_z = 2.4d$  of Naghib-Lahouti *et al.* (2015). The basic intent of this system is to induce spanwise variations in the separated shear layers, such that the vortex street in the turbulent wake regime forms three-dimensionally and is weakened. Synthetic jets upstream of the trailing edge blowing normal to the body are used to force the wake, instead of plasma actuators as in Naghib-Lahouti *et al.* (2015), in order to increase the maximum amplitude of the disturbance. The synthetic jets are located upstream of the trailing edge similar to Naghib-Lahouti *et al.* (2015), but the change in the perturbation from a more streamwise-directed wall jet of a plasma actuator to a more wall-normal type of disturbance from a synthetic jet is expected to affect the forcing effectiveness. Therefore, the present investigation mostly focuses on  $Re_d = 2500$  such that the forcing is most comparable to that of Naghib-Lahouti *et al.* (2015).

A central question to this study is whether this three-dimensional forcing strategy produces an organised or disorganised wake structure. In particular, does distributed forcing generate coherent streamwise vorticity components in the wake, and if so, are they connected to the primary von Kármán vortices, related to vortex dislocations and/or associated with a secondary wake instability? Based on different types of trailing-edge cutouts, Rodríguez (1991) hypothesised that the wake response was essentially associated with how effective the cutouts were at generating streamwise vorticity. With synthetic jet forcing, it is expected that the wake may respond somewhat differently than it does for the various previously investigated means of applying spanwise perturbations. Nevertheless, if the mechanism of distributed synthetic jet forcing is fundamentally related to the development of streamwise vortices in the wake, an objective of this study is to test the hypothesis of Rodríguez (1991) that the drag reduction is tied to the intensity of the streamwise vortices. Active flow control is beneficial for this objective because it allows the forcing amplitude to be easily controlled, unlike with geometrical perturbations.

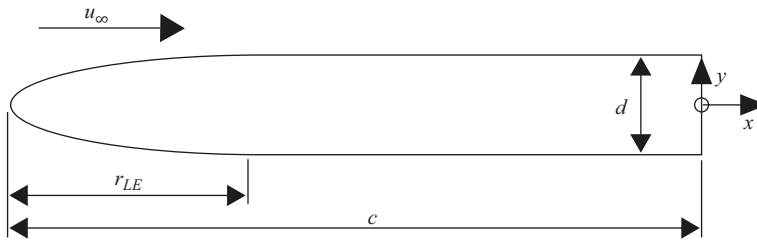


Figure 1. Schematic of a profiled BTE model and coordinate system.

The paper is organised as follows. Section 2 provides the details of the measurement techniques and experiments conducted. Section 3 presents the results and discusses how they answer the research questions. In particular, the interaction of one of the synthetic jets with the cross-flow boundary layer over a range of forcing amplitudes is explored in § 3.1. Spanwise variations induced by forcing in the separated shear layers and the vortex street are then analysed in § 3.2. The three-dimensional structure of the wake is reconstructed in § 3.3. The effect of forcing amplitude on the drag is discussed in § 3.4, and is related back to the wake three-dimensional structure. The conclusions are presented in § 4.

## 2. Methodology

### 2.1. Wind tunnel facility and experimental model

Experimental measurements were made in an open-circuit suction-type wind tunnel at the University of Toronto Institute for Aerospace Studies which has a square cross-section with side lengths of 0.305 m and has a 2.4 m long test section. At free-stream speeds in the range  $1.5 \text{ m s}^{-1} < u_\infty < 6 \text{ m s}^{-1}$ , the turbulence intensity is 0.2%. The BTE model with an elliptical leading edge that is used for the experiments is shown schematically in figure 1. The thickness,  $d$ , of the body is 25.4 mm and the semi-major leading-edge radius,  $r_{LE}$ , is  $2.5d$ . The chord length of the body is  $12.9d$  and it was installed  $22d$  downstream of the start of the test section, with the centre of the model  $6.5d$  above the floor. The model spans the full cross-sectional width of the wind tunnel ( $12d$ ) instead of using endplates. This study investigates  $Re_d = 2500$  and 5000. At these speeds, the boundary layer is laminar when it separates at the trailing edges of the body.

### 2.2. Synthetic jets

Forcing of the flow is provided from an array of synthetic jets, which are located symmetrically on both sides of the BTE-profiled body to give a total of six actuators. They are installed  $1.675d$  upstream of the trailing edges of the body and spaced apart along the span by  $2.4d$ , matching the forcing wavelength investigated by Naghib-Lahouti *et al.* (2015). The synthetic jets are driven by piezoelectric actuators which are clamped inside of separate cylindrical cavities with volumes of approximately  $4000 \text{ mm}^3$ . The nozzle necks of the jets are 2 mm long, leading to rectangular slot exits that are flush with the body surfaces. The slot widths,  $\mathcal{D}$ , are 0.8 mm and the lengths,  $\ell$ , are  $1.2d$  (30.5 mm), giving aspect ratios of 38. The jets issue normal to the body surfaces in the  $y$  direction. The actuators were designed such that the long axis of the slots could be oriented parallel to either the cross-flow direction or the spanwise direction, but only the spanwise configuration is presented in this study. A schematic of the jet arrangement is presented in figure 2.

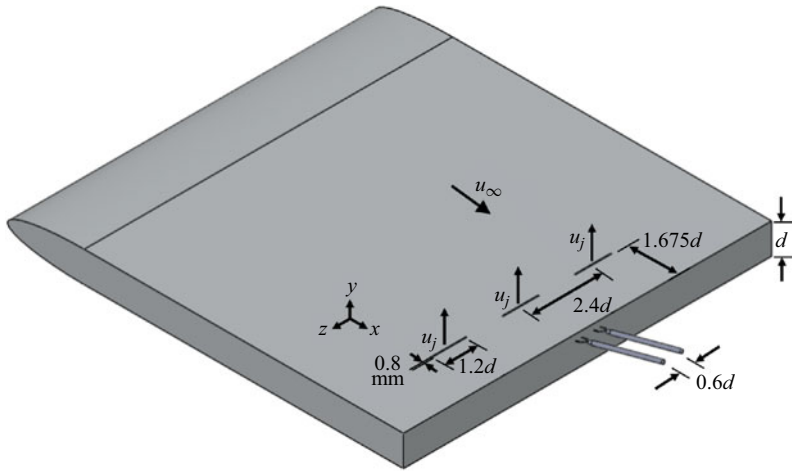


Figure 2. Configuration of the spanwise-oriented synthetic jet array on the BTE-profiled body.

The resonance frequency of the various synthetic jet actuators was experimentally measured as approximately 1500–1800 Hz, and for the forcing experiments, the jets were operated slightly above resonance at a fixed frequency of  $f_j = 2000$  Hz. This frequency is about 130 times greater than the vortex shedding frequency at  $Re_d = 2500$  and about 65 times higher at  $Re_d = 5000$  so the synthetic jet forcing frequency is decoupled from the large-scale structures of the wake. The velocity magnitude of the synthetic jets is quantified as the average velocity in the blowing stroke over the entire cycle (Glezer & Amitay 2002):

$$\bar{u}_j = \frac{1}{T_j} \int_0^{T_j/2} u_j(t) dt, \quad (2.1)$$

where  $T_j = 1/f_j$  is the period. The forcing amplitude can be quantified as both the velocity ratio,  $R$ , and the momentum coefficient,  $C_\mu$ , defined in (2.2) and (2.3) as

$$R = \frac{\bar{u}_j}{u_\infty}, \quad (2.2)$$

$$C_\mu = \frac{N_j \rho \bar{u}_j^2 \ell \mathcal{D}}{u_\infty^2 \lambda_z d} = 2R^2 \frac{\ell \mathcal{D}}{\lambda_z d}, \quad (2.3)$$

where  $\rho$  is the density (same for the jet and the cross-flow) and  $N_j = 2$  is the number of jets per forcing wavelength (two because there are jets on the upper and lower sides of the body). The velocity ratio represents the ratio between the jet velocity magnitude and the free-stream velocity, whereas the momentum coefficient is the ratio of the jet momentum to the effective momentum of the flow over the area being controlled.

The exit velocity of the synthetic jets was measured in the absence of a cross-flow using hot-wire anemometry (HWA). Typically, the hot wire was individually placed at the jet centrelines at a depth of approximately  $0.1\mathcal{D}$  into each slot where the velocity in the expulsion stroke was approximately 10% greater than the velocity during the suction stroke. It was found that the placement of the hot wire at depths ranging from the exit plane to  $0.3\mathcal{D}$  into the slot (corresponding to where the magnitude of the blowing ranged from

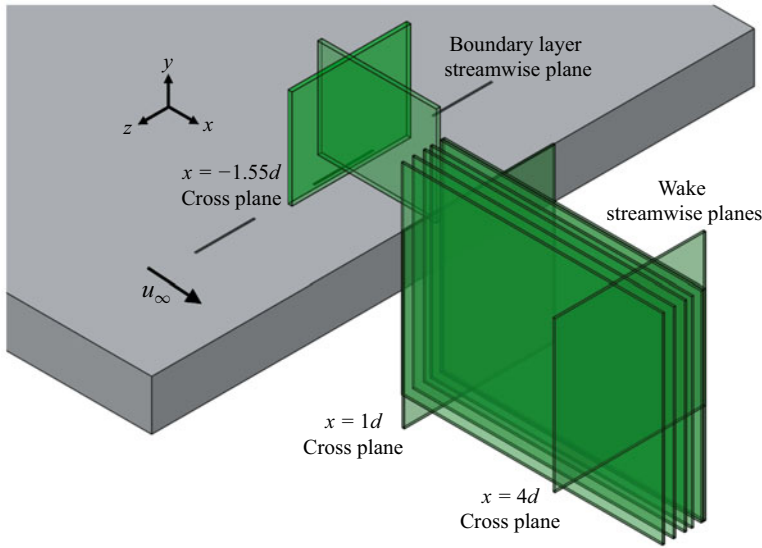


Figure 3. Schematic of the different PIV planes of the boundary layer and wake of the BTE body.

30 % greater to equal to the magnitude of the suction) affected the blowing average velocity by less than 5 % provided that  $\bar{u}_j \geq 4 \text{ m s}^{-1}$  (approximately  $R \geq 2.7$ ). For  $\bar{u}_j < 4 \text{ m s}^{-1}$ , the average blowing velocity was measured to be as much as 8 % higher when the hot wire was positioned at  $0.3D$  in the slot compared with when it was at the exit plane. This was not investigated further as it is considered an acceptable level of uncertainty for the purposes of the present investigation.

For a given excitation voltage, the velocity from each jet was measured simultaneously with the input electrical signal (before amplification) and averaged with respect to the phase of the electrical signal such that  $\bar{u}_j$  could be calculated by (2.1). Each jet was characterised by exciting it with a range of excitation voltages such that  $\bar{u}_j$  typically ranged from 2.5 to at least  $8 \text{ m s}^{-1}$ , which was sufficient to cover the desired forcing amplitudes of this study. The forcing amplitude of the jets was balanced throughout the array for the forcing experiments by providing each jet with a different voltage based on their individual calibrations.

### 2.3. Description of experiments and measurement techniques

The velocity in the boundary layer and wake regions was measured with PIV and HWA. A schematic of the different PIV planes is provided in figure 3. The  $\{x, y\}$  plane is referred to as the streamwise plane. The boundary layer region was measured in a streamwise plane with stereoscopic PIV spanning  $x = -2.1d$  to  $0.1d$  and  $y = 0.515d$  to  $1.9d$  at  $z = 0.05d$ , where  $z = 0$  corresponds to the centreline of the middle jet slot in the array. To measure the wake velocity field, the streamwise PIV planes were positioned symmetrically about  $y = 0$  and with their upstream edge close to the trailing edge of the body. Streamwise-plane two-component (2C)-PIV measurements of the wake were taken at five positions between  $0.05d \leq z \leq 0.82d$ . Stereo PIV measurements were also made in the streamwise wake plane at  $z = 0.08d$ . The  $\{y, z\}$  PIV plane is referred to as the cross-plane and was always viewed stereoscopically. The cross-plane was measured in the boundary layer downstream of the middle jet slot on the upper side of the body at  $x = -1.55d$ . In the wake, it was positioned approximately symmetrically about  $y = 0$

PIV plane field of view	Stereo	$Re_d$	$R$	$C_\mu$	Vector resolution	$f_{\text{samp}}$ (Hz)	$N_{\text{samp}}$	$dt$ ( $\mu\text{s}$ )	Interrogation windows (pixels <sup>2</sup> )
Streamwise boundary layer $x = [-2.1d, 0.1d]$ $y = [0.515d, 1.9d]$ $z = 0.05d$	✓	2500	2.7, 3.1, 3.9	0.23, 0.3, 0.47	$0.009d$	2	400 per phase	20–50	$1.2 \times (512 \times 512)$ $2.2 \times (24 \times 24)$
Streamwise wake $x = [0.3d, 5.5d]$ $y = [-2.0d, 2.0d]$ $z = \{0.05d, 0.24d, 0.38d, 0.6d, 0.82d\}$		2500	3.1	0.3	$0.019d$	2.1	1560	140	$1.2 \times (48 \times 48)$ $2.2 \times (16 \times 16)$
Streamwise wake $x = [0.55d, 6.0d]$ $y = [-2.0d, 2.0d]$ $z = 0.08d$	✓	2500	3.1	0.3	$0.02d$	2	1560	190	$1.1 \times (32 \times 32)$ $2.2 \times (16 \times 16)$
Cross boundary layer $x = -1.55d$ $y = [0.52d, 1.9d]$ $z = [-1d, 0.9d]$	✓	2500	2.7, 3.1, 3.9	0.23, 0.3, 0.47	$0.009d$	2	400 per phase	40–50	$1.2 \times (128 \times 128)$ $2.2 \times (24 \times 24)$
Cross wake $x = 1d$ $y = [-1.9d, 1.5d]$ $z = [-1.5d, 1.5d]$	✓	2500	2.7, 3.1, 3.9	0.23, 0.3, 0.47	$0.033d$	2.5	1040	120	$1.2 \times (64 \times 64)$ $2.2 \times (48 \times 48)$
Cross wake $x = 1d$ $y = [-1.9d, 1.5d]$ $z = [-1.5d, 1.5d]$	✓	5000	1.9, 2.5	0.11, 0.20	$0.033d$	2.5	1040	60	$1.2 \times (64 \times 64)$ $2.2 \times (48 \times 48)$
Cross wake $x = 4d$ $y = [-1.8d, 1.8d]$ $z = [-1.8d, 1.8d]$	✓	2500	1.9, 2.3, 2.7, 3.1, 3.4, 3.5, 3.9, 4.1, 4.4	0.11, 0.17, 0.23, 0.3, 0.36, 0.39, 0.47, 0.52, 0.60	$0.039d$	2.5	1040	100	$1.2 \times (64 \times 64)$ $2.4 \times (48 \times 48)$
Cross wake $x = 4d$ $y = [-1.8d, 1.8d]$ $z = [-1.8d, 1.8d]$	✓	5000	1.0, 1.4, 1.9, 2.1, 2.3, 2.5	0.03, 0.06, 0.11, 0.14, 0.17, 0.20	$0.039d$	2.5	1040	60	$1.2 \times (64 \times 64)$ $2.4 \times (48 \times 48)$

Table 1. Summary of the experimental details, forcing conditions and processing parameters for the various PIV measurements.

and  $z = 0$  at two streamwise positions,  $x = 1d$  and  $x = 4d$ . The effect of a single forcing amplitude of  $R = 3.1$  ( $C_\mu = 0.3$ ) is investigated in the streamwise wake planes and only at  $Re_d = 2500$ , whereas a wider range of forcing amplitudes are explored in the other planes. More specifically, forcing is investigated for  $1.9 \leq R \leq 4.4$  ( $0.11 \leq C_\mu \leq 0.6$ ) at  $Re_d = 2500$  and  $1 \leq R \leq 2.5$  ( $0.03 \leq C_\mu \leq 0.2$ ) at  $Re_d = 5000$  in the wake cross-planes, and the forcing results are examined for  $2.7 \leq R \leq 3.9$  ( $0.23 \leq C_\mu \leq 0.47$ ) at  $Re_d = 2500$  for the boundary layer planes. A summary of the field of views and forcing cases for the PIV measurements is provided in table 1.

The laser beam in all the PIV planes was generated by a dual-pulse Nd-YAG 532 nm Quantel EverGreen laser with 200 mJ energy per pulse. It was directed to the points of interest using a series of mirrors placed on rails outside the wind tunnels. For the boundary layer PIV planes, a 50 mm focal length cylindrical lens was used to spread the

laser sheet and a 1000 mm focal length cylindrical lens was used to narrow its thickness in the fields of view. The laser sheets in the streamwise planes and cross-planes of the wake were formed by a cylindrical lens with a focal length of 25 mm and a 500 mm focal length spherical lens. The thickness of the laser sheet in the respective field of views was 1–2 mm. The lasers sheets illuminated di(2-ethylhexyl)sebacate particles that were seeded homogeneously into the flow by a LaVision aerosol generator. The PIV system was managed using LaVision FlowMaster hardware and software. The images were acquired by LaVision Imager sCMOS cameras which have resolutions of 2560 pixels by 2160 pixels and 16-bit dynamic range. AF Micro-Nikkor 60 mm lenses with the apertures set to  $f/2.8$  were used for the streamwise wake planes, Sigma EX DG 105 mm lenses at  $f/4$  were used for the wake cross-planes, and Sigma EX DG 105 mm lenses with 15 mm extension tubes, with the apertures at  $f/11$ , were used for the boundary layer planes. To minimise the intensity of spurious laser reflections seen by the cameras, the back face of the model was painted with a rhodamine–acrylic mixture for the wake PIV measurements and graphic film was taped around the back surface of the body for the boundary layer PIV measurements, and in all cases the camera lenses were outfitted with narrow bandpass 532 nm filters.

For the wake streamwise plane PIV measurements, the laser sheet entered the wind tunnel from the bottom. The camera was positioned normal to the streamwise 2C-PIV wake measurement planes. The cameras were located on opposite sides of the light sheet for the stereo PIV measurements in the streamwise plane of the wake and viewed at  $34^\circ$  and  $38^\circ$  angles relative to the normal of the laser plane. For the cross-plane wake PIV measurements, the two cameras were both located downstream of the laser plane (which entered from the side), viewing the flow from above and below the wind tunnel, respectively. At  $x = 1d$ , the angles of the cameras were at  $45^\circ$  and  $47^\circ$  with respect to the normal of the laser plane, whereas at  $x = 4d$ , the angles were  $28^\circ$  and  $45^\circ$ . The laser sheet for both the streamwise and cross-plane boundary layer PIV measurements entered from a side of the wind tunnel. The cameras for the streamwise PIV plane in the boundary layer were located on opposite sides of the wind tunnel at angles of  $44^\circ$  and  $49^\circ$  with respect to the normal of the laser plane. For the cross-plane measurements, the cameras were also on opposite sides of the wind tunnel, with one camera at  $60^\circ$  and the other at  $64^\circ$  from the normal of the laser plane. Scheimpflug adapters were installed between the lenses and camera sensors, and were angled such that the particles were in focus throughout the images.

The acquisition frequencies of the snapshots, listed in [table 1](#), are non-integer multiples of the frequencies of the relevant flow structures – in particular, vortex shedding – and so the images are considered to be asynchronous with respect to the large-scale structures. The snapshots in the boundary layer PIV planes were taken phase-locked at two phases with respect to the jet forcing cycle (2000 Hz). The reference signal for phase locking was the input voltage signal to the piezoelectric actuators. The phase difference between the jet output velocity and the driving voltage was measured from the synthetic jet calibration. If  $\phi_j = 0^\circ$  is defined as the start of the blowing cycle and  $\phi_j = 90^\circ$  is peak blowing, then the phases measured are  $\phi_j = 78^\circ$  (near peak blowing) and  $\phi_j = 258^\circ$  (near peak suction). For the wake PIV planes, the snapshots were acquired irrespective of the phase of the synthetic jets. The pulse delay,  $dt$ , between the snapshot pairs is also summarised in [table 1](#) for the various planes. It was set such that the maximum particle displacements were approximately 5–8 pixels in all planes. The PIV images for the stereo wake streamwise plane and the wake cross-planes were processed with DaVis 8.4, whereas DaVis 11 was used for the 2C-PIV wake streamwise planes and the boundary layer plane measurements. The raw images were pre-processed to remove background noise. The velocity vector fields

were calculated from the PIV images using a sequential cross-correlation algorithm with multiple passes in DaVis. Table 1 lists the initial and final size of the interrogation windows as well as the number of passes in the processing. The final pass had interrogation windows that were  $24 \times 24$  pixels<sup>2</sup> for the boundary layer planes,  $16 \times 16$  pixels<sup>2</sup> for the streamwise wake planes and  $48 \times 48$  pixels<sup>2</sup> for the wake cross-planes, all with 50% overlap. The instantaneous velocity fields were post-processed to remove outlying vectors which were identified using global (from time-averaged statistics) and local (based on median spatial filters constructed from instantaneous fields) metrics. Rejected vectors were replaced with bilinear interpolation. Uncertainties of the statistics derived from the PIV measurements were calculated with a bootstrapping approach (Efron 1979).

Analogue signals were collected using a National Instruments PCI-6259 data acquisition card through an SCC-68 terminal block. Hot-wire anemometry was employed using a StreamLine 90N10 CTA system with StreamWare v1.17 software. Straight single-wire Dantec 55P01 probes were used, modified in house utilising copper-plated tungsten wire. The sensing elements were  $5 \mu\text{m}$  in diameter and approximately 1–1.5 mm long. The system was operated at an overheat ratio of 0.6 for all the measurements of the wake. The hot wires were oriented tangentially to the  $z$  direction and with the probes at approximately  $15^\circ$  relative to the horizontal. The wires that were used to make measurements in the wind tunnel were calibrated *in situ* using the velocity calculated from pitot-static probe pressure measurements in the free stream as the reference. A MKS Baratron 225A 1 Torr transducer was connected to both sides of the pitot-static probe for the experiments. The accuracy of the pressure measured with the MKS Baratron 225A transducer is 0.5% of full scale. The reference velocities for the synthetic jet characterisation were provided by a StreamLine 90H02 flow unit. Hot-wire calibration curves for the wake measurements were constructed from 12 mean reference velocity data points that were logarithmically distributed from approximately 1 to  $10 \text{ m s}^{-1}$ . A King's law curve fit was employed to relate the measured voltage to velocity. The ambient temperature was measured with a J-type thermocouple. The temperature was allowed to drift up to  $1^\circ\text{C}$  from the temperature at which the bridge was balanced. The measured voltages from the hot wires were temperature-corrected using the methodology of Hultmark & Smits (2010) to account for changes in the ambient temperature. The systematic uncertainty associated with hot-wire calibration is estimated to be 3% based on the methodology of Yavuzkurt (1984).

The hot wires were positioned in the wake by a three-axis traverse system. Velocity profiles of the separated shear layers at  $x = 0.2d$  from  $0.35 \leq y \leq 1.8d$  and along  $0 \leq z \leq 1.1d$  were measured over the ranges of  $Re_d = 2500$  ( $2.3 \leq R \leq 3.2$ ),  $Re_d = 3700$  ( $1.8 \leq R \leq 2.3$ ) and  $Re_d = 5000$  ( $1.4 \leq R \leq 1.9$ ). This was accomplished with hot wires spanwise-separated by  $0.6d$  that simultaneously sampled the flow (see figure 2). Another spanwise scan was done at  $\{x = 4.5d, y = -0.8d\}$  along  $0 \leq z \leq 1.1d$  at  $\{Re_d = 2500; R = 3.1 \text{ and } 3.9\}$ , also with two hot wires spanwise-separated by  $0.6d$ . All the points measured with HWA were sampled for 120 s at 25 kHz, with an analogue 10 kHz low-pass filter to prevent aliasing.

### 3. Results and discussion

#### 3.1. Interaction of a synthetic jet with the boundary layer

This investigation begins by examining the PIV measurements of a synthetic jet issuing into the boundary layer of the BTE-profiled body. Although the primary region of interest in this study is the wake, the von Kármán vortex street develops from the separated shear layers, which themselves can be envisioned as continuations of the boundary layers

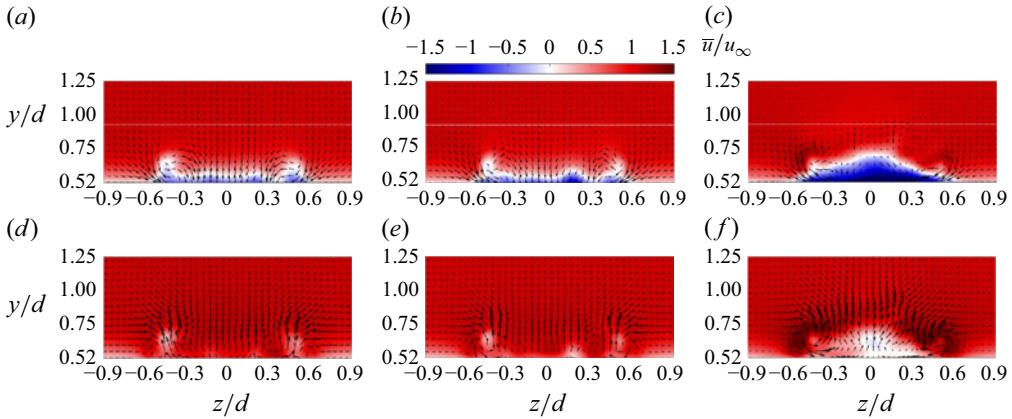


Figure 4. Streamwise velocity field with  $(v, w)$  vectors in the cross-plane at  $x = -1.55d$ , averaged at constant phases of the synthetic jet oscillation cycle at  $Re_d = 2500$ : (a)  $\phi_j = 258^\circ$ ,  $R = 2.7$ , (b)  $\phi_j = 258^\circ$ ,  $R = 3.1$ , (c)  $\phi_j = 258^\circ$ ,  $R = 3.9$ , (d)  $\phi_j = 78^\circ$ ,  $R = 2.7$ , (e)  $\phi_j = 78^\circ$ ,  $R = 3.1$  and (f)  $\phi_j = 78^\circ$ ,  $R = 3.9$ .

developed over the body. Because the synthetic jets issue into the boundary layers and force the wake via the boundary layers, it is important to understand the jet–boundary layer interaction to interpret the effects on the vortex shedding.

The blowing of a jet in a cross-flow results in a momentum exchange between the jet and the surrounding fluid and generates a wide variety of coherent vortical structures (Fric & Roshko 1994). Commonly, the downstream flow of a jet in cross-flow is dominated by a counter-rotating vortex pair (Karagozian 2014). However, the jet trajectory and the particular vortical structures formed are strongly dependent on the relative strength of the jet as well as the jet geometry/orientation (Tricouros, Amitay & Van Buren 2023). For a pulsed or synthetic jet, the frequency also significantly impacts the types of vortical structures (Eroglu & Breidenthal 2001; Jabbal & Zhong 2008; Sau & Mahesh 2008). The focus of the present study is not to map this wide parameter space, but to investigate specific forcing amplitudes that are important for distributed forcing with the current jet geometry. Because the jet geometry is fixed, the interpretation of the results in the present study is not affected by whether  $R$  or  $C_\mu$  is used to characterise the forcing amplitude. However, for this study,  $R$  is preferred over  $C_\mu$  because  $R$  characterises only the strength of the forcing at a particular spanwise position along the jet, whereas  $C_\mu$  incorporates both the relative momentum flux at a particular position and the area that the jet acts over. Hence, characterising the forcing amplitude with  $C_\mu$  makes an assumption that  $\ell$  and  $\mathcal{D}$  are equally important, which cannot be tested from the present results. The focus of this section is on velocity ratios of  $R = \{2.7, 3.1 \text{ and } 3.9\}$  at  $Re_d = 2500$ .

Figures 4 and 5 present the streamwise velocity and spanwise vorticity fields, respectively, in the cross-plane at  $x = -1.55d$  ( $0.125d$  downstream of a jet slot) averaged at constant phases with respect to the synthetic jet oscillation cycle for the selected forcing amplitude cases. Figure 4(a–c) shows the field near the suction peak at  $\phi_j = 258^\circ$  and figure 4(d–f) that averaged near the blowing peak at  $\phi_j = 78^\circ$ . The measurements in this near-field region of the jet show a clear cyclic variation of the velocity at the forcing frequency. In particular, the  $\bar{v}$  component in the centre region of the slot near the wall ( $|z| \leq 0.3d$ ,  $y \leq 0.7d$ ) is directed towards the wall during the suction part of the cycle and vice versa during the blowing part of the cycle. Additionally, there is a significant spanwise gradient of  $\bar{v}$  near the edges of the slot from  $0.3d \leq |z| \leq 0.6d$  at all phases

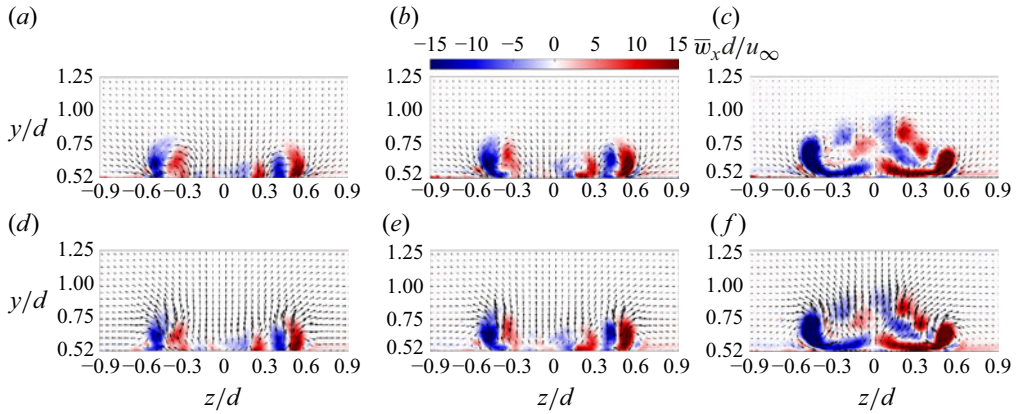


Figure 5. Spanwise vorticity field with  $(v, w)$  vectors in the cross-plane at  $x = -1.55d$ , averaged at constant phases of the synthetic jet oscillation cycle at  $Re_d = 2500$ : (a)  $\phi_j = 258^\circ$ ,  $R = 2.7$ , (b)  $\phi_j = 258^\circ$ ,  $R = 3.1$ , (c)  $\phi_j = 258^\circ$ ,  $R = 3.9$ , (d)  $\phi_j = 78^\circ$ ,  $R = 2.7$ , (e)  $\phi_j = 78^\circ$ ,  $R = 3.1$  and (f)  $\phi_j = 78^\circ$ ,  $R = 3.9$ .

of the cycle. This is indicative of the development of edge streamwise vortices, seen directly in figure 5, which is a characteristic feature of rectangular synthetic jets that issue normal to the wall (Van Buren *et al.* 2016). The sense of rotation of the streamwise vortices is such that fluid is lifted away from the wall in the jet centreline region and brought towards the wall in the regions near the slot edges. These streamwise vortices may be expected to convect downstream and to redistribute the momentum in the boundary layer, energising the regions close to the jet slot edges with higher-velocity fluid from the outer part of the boundary layers and vice versa in regions more closely aligned with the jet centreline. If the changes in the flow field between phases (time) at  $x = -1.55d$  are primarily driven by the downstream convection of coherent structures through this plane, then the phase dependence could be converted into spatial information through Taylor’s hypothesis. However, the streamwise vorticity in this plane does not appear to significantly change during the cycle in spite of the significant phase variation of  $\bar{u}$  near the jet edges because the average gradients in  $y$  and  $z$  remain relatively constant during the cycle. This implies that Taylor’s hypothesis cannot be applied in this plane. During the suction phase of all the investigated cases,  $\bar{u}$  points upstream near the wall in the  $x = 1.55d$  plane, which is consistent with the jet ingesting the boundary layer fluid at this phase of the cycle. However, the region of reversed flow is notably larger in the  $R = 3.9$  case compared to the lower- $R$  cases at  $Re_d = 2500$ . Indeed, there is negative  $\bar{u}$  in the  $x = 1.55d$  plane even during the blowing part of the cycle. This is indicative of the jet in the  $R = 3.9$  case having sufficient strength to block the incoming boundary layer and highlights a change in the jet–boundary layer interaction.

The interaction of the jet and the boundary layer and its propagation downstream can be better seen in the streamwise plane over a jet slot. Figure 6 shows the velocity/vorticity fields without forcing and for the selected forcing cases in the streamwise plane at  $z = 0.05d$ . The forcing results are again presented near the suction peak at  $\phi_j = 258^\circ$  for figure 6(b–d) and near the blowing peak at  $\phi_j = 78^\circ$  for figure 6(e–g). Without forcing (figure 6a), the boundary layer thickness is approximately  $0.3d$  at  $Re_d = 2500$ ; the boundary layer shear manifests as significant negative spanwise vorticity on the upper side of the body up to  $y \approx 0.75d$ . For a rectangular synthetic jet issuing in quiescent conditions, a vortex ring would be expected to be generated during the blowing phase, producing opposite-sign vorticity components at the opposite sides of the slot (Van Buren,

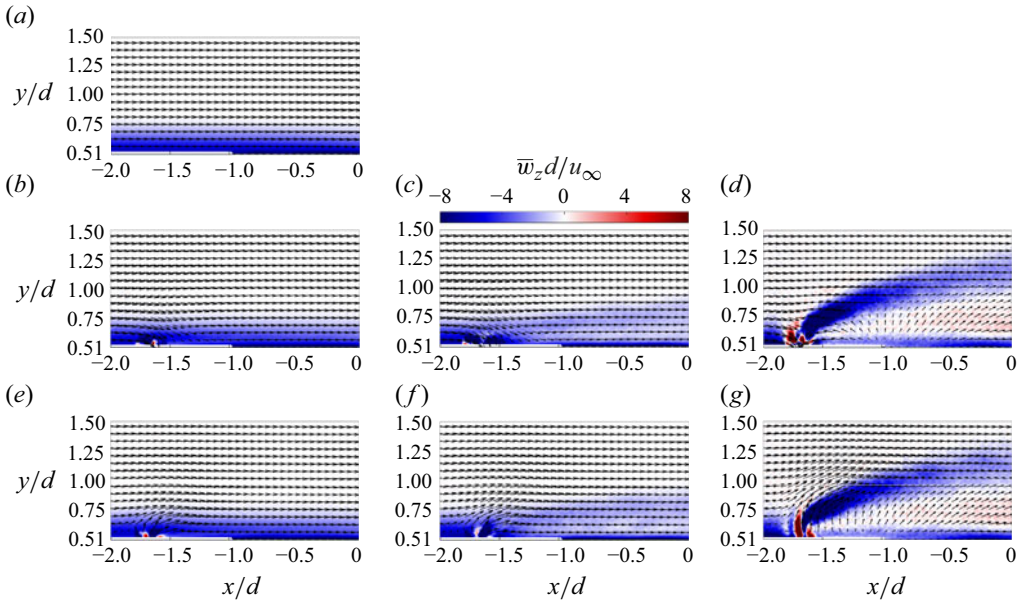


Figure 6. Spanwise vorticity field with  $(u, v)$  vectors in the streamwise plane at  $z = 0.05d$ , averaged at constant phases of the synthetic jet oscillation cycle at  $Re_d = 2500$ : (a) no forcing, (b)  $\phi_j = 258^\circ$ ,  $R = 2.7$ , (c)  $\phi_j = 258^\circ$ ,  $R = 3.1$ , (d)  $\phi_j = 258^\circ$ ,  $R = 3.9$ , (e)  $\phi_j = 78^\circ$ ,  $R = 2.7$ , (f)  $\phi_j = 78^\circ$ ,  $R = 3.1$  and (g)  $\phi_j = 78^\circ$ ,  $R = 3.9$ .

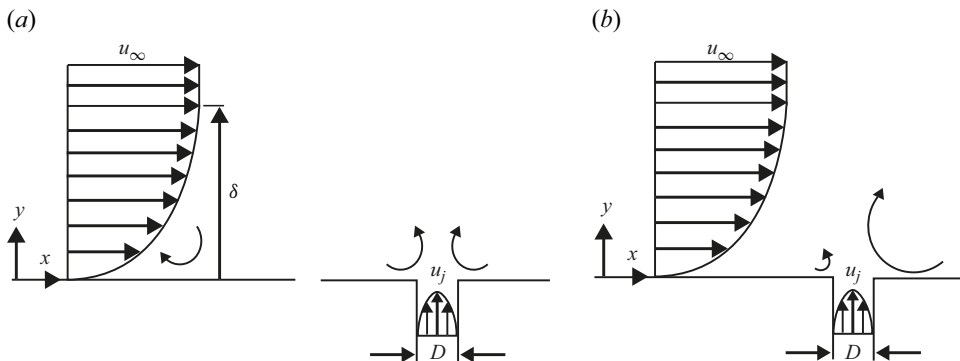


Figure 7. Sketch of the dominant spanwise vorticity components from the boundary layer and a synthetic jet (during the blowing phase). (a) The vorticity from the boundary layer and synthetic jet is shown separately. (b) The synthetic jet is shown issuing into the boundary layer, which causes the vortex on the upstream side of the jet either to be cancelled or to get weaker and the vortex on the downstream side to get stronger.

Whalen & Amitay 2014). This is sketched in figure 7(a). When a cross-flow boundary layer is introduced, the shear from the boundary layer opposes the positive-sign jet vorticity that would be generated on the upstream side of the slot in quiescent conditions. In the  $R = 2.7$  and  $R = 3.1$  cases at  $Re_d = 2500$ , the boundary layer is still largely dominated by negative spanwise vorticity, indicating that the jet vorticity on the upstream side is mostly cancelled except for some localised regions just upstream of the slot during the blowing phase, as sketched in figure 7(b). In the  $R = 3.9$  case, a much larger region of  $+\bar{w}_z$  can be observed on the upstream side during the blowing phase that extends up to  $y \approx 0.75d$ , indicating that the jet is sufficiently strong to overcome the boundary layer vorticity. This

observation is similar to that of Jabbal & Zhong (2008) for a synthetic jet emanating from a circular orifice and that of Sau & Mahesh (2008) for a pulsed circular jet. In particular, Jabbal & Zhong (2008) found that the structures formed by their synthetic jet changed from hairpin vortices to distorted vortex rings when  $R$  reached a critical amplitude. The distorted vortex rings generated by Jabbal & Zhong (2008) penetrated much more deeply through the boundary layer than the hairpin vortices, which can be attributed to the inherent self-induced velocity pointing away from the wall of vortex rings. In the present study, coherent vortex rings are not evident from the synthetic jet slot in the cross-flow, consistent with the observations of Van Buren *et al.* (2016) for rectangular synthetic jets. Van Buren *et al.* (2016) attributed the absence of vortex rings to them breaking up almost immediately after they form. However, the considerable phase-coherent fluctuations at the forcing frequency in the near field of the jet are indicative of some type of coherent structure. Theoretically, if the phase-coherent fluctuations are carried by vortices of  $\mathcal{O}(D)$ , this would correspond to only about three vectors at the current resolution. The fact that these small-scale structures are not directly evident in the PIV flow fields suggests that they are simply too small and closely packed to be resolved from the current measurements. It can be seen in figure 6 that the emergence of positive vorticity at the upstream side of the slot is associated with a considerable increase in the jet penetration compared with the lower- $R$  cases. This suggests that the emergence of a significant concentration of positive vorticity at the upstream side of the slot has a similar effect to the self-induced velocity from an actual vortex ring.

In all the forcing cases, the jets cause a streamwise velocity deficit downstream of the slots. This can be attributed to at least two different fundamental mechanisms. Firstly, the jets have a blockage-like effect because the fluid coming out from the plane of the slot is initially pointed in the wall-normal direction. Therefore, the jet transfers its wall-normal momentum to the cross-flow. By the same token, the cross-flow transfers some streamwise momentum to the jet fluid, causing the fluid downstream of the slot to slow down and the jet bends in the direction of the cross-flow until a new equilibrium is reached. Secondly, the streamwise vortices generated at the edges of the synthetic jet slots (see figure 5) are rotating in a direction to cause the low-momentum fluid aligned with the jet centreline plane to move away from the wall (Rathnasingham & Breuer 2003). The wake-like region downstream of the slot in the  $z = 0.05d$  streamwise plane is more evident for the  $R = 3.1$  case compared with  $R = 2.7$  when  $Re_d = 2500$ . This is consistent with the jets in the  $R = 3.1$  case penetrating deeper into the cross-flow and convecting downstream closer to the jet centreline plane, similar to the flow fields presented by Van Buren *et al.* (2016) for a rectangular spanwise-oriented synthetic jet. The  $R = 3.9$  case has a significantly larger wake-like region downstream of the slot than the lower- $R$  cases at this  $Re_d$  because the jet is sufficiently strong to cause the incoming boundary layer to completely separate. Consequently, the shear layer along the jet centreline plane splits into two parts: an inner region associated with the boundary layer as it recovers downstream, and an outer region associated with the penetrating jet above which the flow finally reaches the free stream. Notably, the phase coherence of the fluctuations at the jet frequency disappears downstream of  $x \approx -0.5d$ , or  $\approx 35D$  downstream of the slot. The loss of phase-coherent fluctuations as a synthetic jet evolves downstream has been used as an indication of the transition between the near field and far field of the jet-cross-flow interaction by Van Buren *et al.* (2016), where they estimated this transition happened at approximately  $20D$  downstream of their jets. In the present case, the loss of phase-coherent high-frequency jet fluctuations upstream of the trailing edge further highlights that the perturbations to the wake from the synthetic jets can justifiably be considered as steady with respect to the energy-containing structures of the wake. Importantly, these results indicate that the

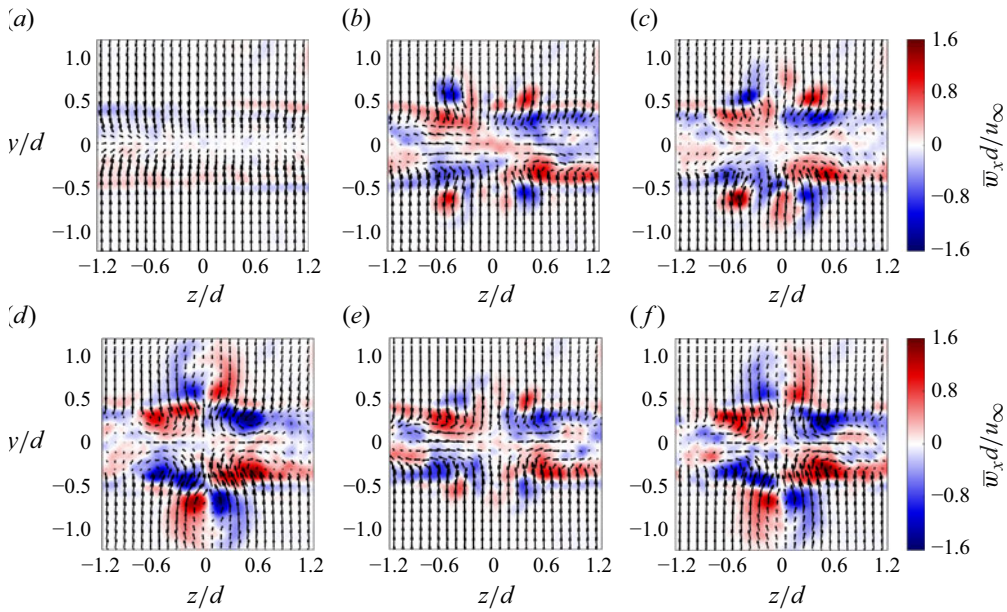


Figure 8. Mean streamwise vorticity field with  $(v, w)$  vectors in the cross-plane at  $x = 1d$  with (a)  $\{Re_d = 2500, \text{ no forcing}\}$ , (b)  $\{Re_d = 2500, R = 2.7\}$ , (c)  $\{Re_d = 2500, R = 3.1\}$ , (d)  $\{Re_d = 2500, R = 3.9\}$ , (e)  $\{Re_d = 5000, R = 1.9\}$  and (f)  $\{Re_d = 5000, R = 2.5\}$ .

forcing from the array of synthetic jets is capable of significantly perturbing the boundary layers.

### 3.2. Spanwise variation in the wake structure

The cross-plane in the near wake is studied next in order to observe the spanwise variations in the wake upstream of vortex street formation that are induced by the distributed forcing. **figure 8** shows the distributions of the mean streamwise vorticity,  $\bar{\omega}_x$ , at  $x = 1d$  for the unforced case at  $Re_d = 2500$ , as well as with forcing at  $\{Re_d = 2500; R = 2.7, 3.1 \text{ and } 3.9\}$  and  $\{Re_d = 5000; R = 1.9 \text{ and } 2.5\}$ . At this location, the shear layers are rolling up and so it is at approximately the end of what one could call the separated shear layer region. Without forcing,  $\bar{\omega}_x$  is very low in this plane because the time-averaged wake is approximately spanwise uniform. Nevertheless, it should be appreciated that the wake is turbulent and exhibits instantaneous three-dimensional features, such as small-scale coherent streamwise vortices (Gibeau, Koch & Ghaemi 2018), but they are not observed in **figure 8(a)** because of the time-averaging.

Coherent streamwise vortices are evident in the cross-plane mean field of the forced cases. On each side of the body, there are two pairs of streamwise vortices in the  $x = 1d$  plane: one set that is biased towards the free-stream side of the separated shear layers at  $|y| > 0.5$ , and another set at  $|y| < 0.4d$  inside the recirculation region. In accordance with the matched forcing amplitude from all the jets and symmetric placement of the actuators on both sides of the body, the perturbations in the mean fields exhibit vertical symmetry about  $y = 0$  and spanwise symmetry about  $z = 0$ . The vortex pairs that are located at  $|y| > 0.5$  are consistent with the jet edge streamwise vortices shown in **figure 5**. The sense of rotation of the vortices is such that outboard of the vortices, the higher velocity flow from the free stream is brought lower into the boundary layer, and vice versa for the region inboard of the vortices closer to the jet centreline ( $z = 0$ ). Hence, it can be surmised that

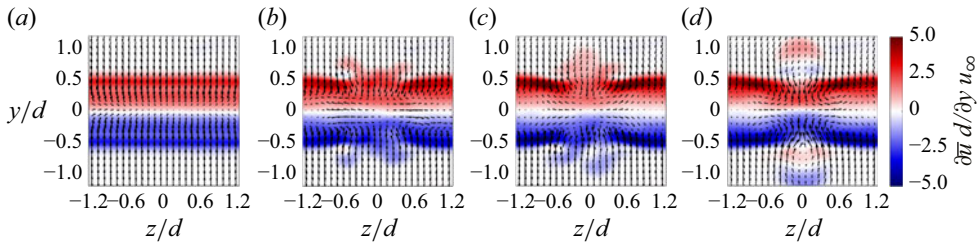


Figure 9. The  $\partial\bar{u}/\partial y$  field with  $(v, w)$  vectors in the cross-plane at  $x = 1d$  when  $Re_d = 2500$  with (a) no forcing, (b)  $R = 2.7$ , (c)  $R = 3.1$  and (d)  $R = 3.9$ .

these vortices redistribute momentum in the boundary layer and near wake as they convect downstream.

The jet edge vortices of the  $\{Re_d = 2500, R = 2.7\}$  and  $\{Re_d = 5000, R = 1.9\}$  cases are located close to the jet slot edge plane. They are centred at  $|y| \approx 0.5d - 0.55d$  but extend up to  $|y| \approx 0.75d$  in the  $\{Re_d = 2500, R = 2.7\}$  case and to  $|y| \approx 0.6d$  in the  $\{Re_d = 5000, R = 1.9\}$  case. The boundary layer thickness is approximately  $0.3d$  and  $0.21d$ , respectively, at  $Re_d = 2500$  and  $5000$ , so these vortices are approaching the edge of the boundary layer but are not penetrating beyond. In the  $\{Re_d = 2500, R = 3.1\}$  case, the edge streamwise vortices on the  $|y| > 0.5$  side are still mostly concentrated at  $|y| < 0.8$ , but there are small amounts of streamwise vorticity outside of  $|y| > 0.8$  in the jet centreline region, indicating that the streamwise vortices are penetrating right up to the edges of the boundary layers. In the  $\{Re_d = 2500, R = 3.9\}$  and  $\{Re_d = 5000, R = 2.5\}$  cases, the streamwise vortices formed by the jet–boundary layer interaction are larger and can be seen to be extending outside the boundary layers. For these relatively higher-forcing-amplitude cases, the pairs of vortices are more closely spaced, consistent with the findings of Van Buren *et al.* (2016) for spanwise-oriented synthetic jet slots. The fact that this occurs at a much lower  $R$  when  $Re_d = 5000$  compared with  $Re_d = 2500$  suggests that  $R$  (or  $C_\mu$ ) is not a very appropriate way to scale the forcing amplitude across different  $Re_d$  for this type of forcing. An alternative way of scaling the forcing amplitude that provides a better collapse over different  $Re_d$  is proposed in § 3.3.

Figure 8 shows that on the free-stream sides of the separated shear layers ( $|y| > 0.5$ ), the jet edge vortices direct the flow along  $z$  towards the jet centreline plane. Inside the recirculation region ( $|y| < 0.4d$ ), the flow points in the opposite direction, away from the jet centreline plane. This forms a set of induced streamwise vortices which have the opposite sense of rotation to that of the jet edge vortices. Although  $\omega_z$  cannot be directly calculated from a cross-plane, the  $\partial\bar{u}/\partial y$  field should be representative of the trends of the  $\bar{\omega}_z = (\partial\bar{v}/\partial x - \partial\bar{u}/\partial y)$  field at  $x = 1d$  because it is still relatively close to the trailing edge. Figure 9 plots  $\partial\bar{u}/\partial y$  in the  $x = 1d$  cross-plane for the  $\{Re_d = 2500; R = 0, 2.7, 3.1 \text{ and } 3.9\}$  cases. When the forcing amplitude is at  $R = 3.1$ , the greater penetration of the jets as compared with  $R = 2.7$  causes the shear layer thickness to increase more in the inboard region of the wake, as can also be seen in figure 6. The  $R = 3.9$  case can be contrasted to the lower- $R$  cases at  $Re_d = 2500$  by the presence of two distinct regions in the shear layers in the inboard region of the slots. This is consistent with the vorticity field of figure 6(d,g), and can be attributed to the boundary layers completely separating when they encounter the jet slots when  $R = 3.9$  at  $Re_d = 2500$ , thereby allowing the jets to penetrate outside of the boundary layers. This increases the width of the wake inboard of the slots and can be expected to result in a higher drag compared with the  $R = 2.7$  and  $R = 3.1$  cases at  $Re_d = 2500$  because the momentum deficit grows

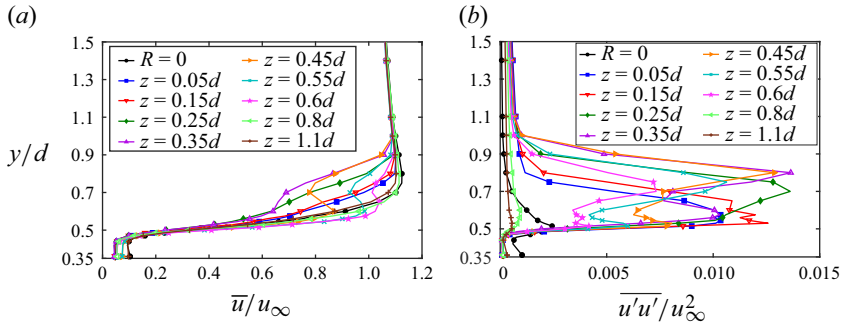


Figure 10. Selected shear layer profiles along the span at  $x = 0.2d$  for  $\{Re_d = 2500, R = 3.1\}$ , measured using HWA: (a)  $\bar{u}/u_\infty$ ; (b)  $\overline{u'u'}/u_\infty^2$ .

when the wake is wider. Therefore, it can be surmised that the forcing amplitude that achieves the best drag reduction should be a compromise between increasing the spanwise variations in the wake without causing it to significantly widen anywhere along the span.

Figure 10 shows profiles of  $\bar{u}/u_\infty$  and  $\overline{u'u'}/u_\infty^2$  in the upper separated shear layer at various locations along the span for the  $\{Re_d = 2500, R = 3.1\}$  case at  $x = 0.2d$ , where the approximation that  $-\partial\bar{u}/\partial y$  is representative of  $\bar{\omega}_z$  should be more valid. It can be seen that the shear layer varies significantly along the span in the forced cases. Generally, the velocity gradient along  $y$  at  $y = 0.5d$  is less steep in the  $|z| \leq 0.35d$  profiles and more concentrated from  $|z| \geq 0.45d$  compared with the unforced case. For this case, the shear layer is least concentrated, i.e. at its thickest, from  $0.25d \leq z \leq 0.35d$ . The spanwise variations in the shear layer thickness are driven by the combined effect of the jet blockage and the regions of upwash and downwash associated with the streamwise vortices that redistribute the momentum in the boundary layers. The influence of the jet edge vortices can be clearly seen in the  $z = 0.45d$  and  $0.55d$  shear layer profiles of the  $\{Re_d = 2500, R = 3.1\}$  case, where there is a velocity deficit in the outer region of the shear layer and accelerated velocity closer to  $y = 0.5d$ . The profile at  $z = 0.8d$  also exhibits a steeper velocity gradient along  $y$ , but the effect diminishes moving away from the slot towards  $z = 1.1d$ .

Given that vortex shedding is periodic, further insight into the origin of the streamwise vortices in the  $x = 1d$  cross-plane can be gained by phase-averaging the measurements. Using the methodology outlined in Appendix A, the phase reference for this plane is based on the relationship between the  $u$  and  $v$  components in the instantaneous snapshots at  $\{x, y\} = \{1d, \pm 1.05d\}$ , averaged across the spanwise domain of the snapshots. This methodology is possible because the turbulent velocity fluctuations are not very large in this part of the wake and the  $u$  and  $v$  components are periodically modulated by the passage of the von Kármán vortices. The snapshots in the  $x = 1d$  plane for the  $\{Re_d = 2500, R = 3.1\}$  case were sorted with respect to the phase reference into 12 phase bins. For a given shedding phase bin,  $\phi_v$ , composed of  $N_\phi$  samples, the phase-averaged velocity is calculated as

$$\tilde{u}(\phi_v) = \sum_{i=1}^{N_\phi} \frac{u_i(\phi_v)}{N_\phi}, \quad (3.1)$$

adopting a notation where phase-averaged statistics are denoted with a tilde. The streamwise vorticity fields of the  $\{Re_d = 2500, R = 3.1\}$  case at two different shedding

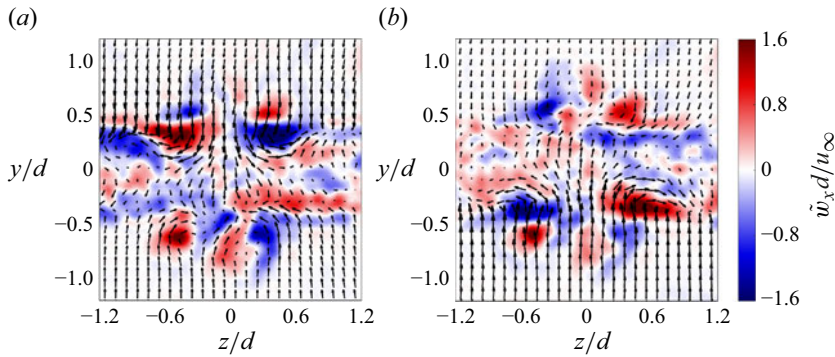


Figure 11. Streamwise vorticity fields and  $(v, w)$  vectors for the  $\{Re_d = 2500, R = 3.1\}$  case in the  $x = 1d$  plane at  $(a,b)$  two different phases ( $180^\circ$  apart) of the shedding cycle.

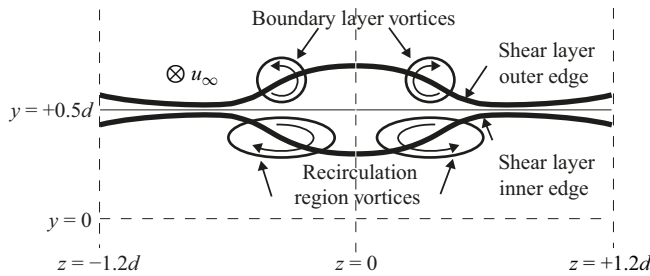


Figure 12. Sketch of the vortical structures induced by forcing in the separated shear layer from the  $y > 0$  side of the body.

phases  $180^\circ$  apart are shown in [figure 11](#). Throughout the shedding cycle, the streamwise vortex pairs at  $|y| > 0.5d$  are relatively stable in strength and location in this plane. Their consistency can be attributed to the synthetic jets operating at a much higher frequency than the vortex shedding. Hence, the steadiness of these vortices over the shedding cycle is another indication that the outer-region vortex pairs originate from the jet–boundary layer interaction and convect into the wake. In contrast, the streamwise vortices in the recirculation region periodically alternate between the upper and lower sides of the wake during the cycle, indicating a much closer connection to the wake dynamics. The phases presented in [figures 11\(a\)](#) and [11\(b\)](#) correspond to when these vortices are at maximum strength in the upper and lower sides of the wake, respectively.

[Figure 12](#) presents a sketch of the mean flow field in the near wake, showing the spanwise variation of the shear layer thickness and coherent vortices based on [figures 8](#) to [11](#). The process by which the spanwise variations in the shear layers affect the vortex shedding and periodically induce streamwise vortices to form can be illustrated by considering the vorticity transport equation for incompressible flow, neglecting viscous diffusion:

$$\frac{D\omega_i}{Dt} = \omega_\kappa \frac{\partial u_i}{\partial x_\kappa}, \quad (3.2)$$

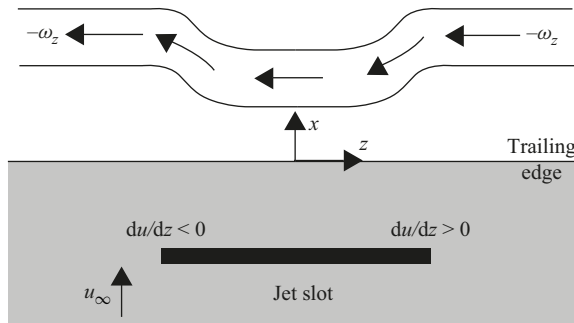


Figure 13. Sketch of the tilting of the spanwise vorticity shed from the upper side of the body due to spanwise gradients in the streamwise velocity in the shear layer, from a top view.

and for the streamwise component, this can be decomposed as

$$\frac{D\omega_x}{Dt} = \omega_x \frac{\partial u}{\partial x} + \omega_y \frac{\partial u}{\partial y} + \omega_z \frac{\partial u}{\partial z}. \quad (3.3)$$

Special attention is drawn to the  $\omega_z(\partial u/\partial z)$  vortex tilting term because of the inherently large  $\omega_z$  concentrations which compose the separated shear layers and from which the von Kármán vortices develop. The establishment of spanwise gradients in the streamwise velocity inside the separated shear layers provides the condition necessary to tilt the spanwise von Kármán vortices into the streamwise direction and to cause gradients in the spanwise vorticity along the span. It is noted that conservation of circulation requires the generation of streamwise vorticity through the diversion of spanwise vorticity to be associated with a corresponding reduction in the overall spanwise circulation. The process of shear layer tilting on the upper side of the body is sketched in figure 13. The region of  $\partial u/\partial z < 0$  in the separated shear layer on the  $z < 0$  side of the jet creates  $+\omega_x$ , and vice versa for the other side. Hence, the direction of the tilting of the spanwise vorticity is such that the von Kármán vortices are retarded in the inboard region of the jet slots as they shed. The sense of rotation of the streamwise vortices within the recirculation region in figures 8 and 11 and that are sketched in figure 12 are consistent with this vortex street rollup pattern. As a von Kármán vortex from one side of the body is developed, the streamwise vortex pair that is developed due to the tilting of the vorticity of the separated shear layer also grows. Then, the streamwise vorticity declines on that side of the body after the von Kármán vortex sheds while the reverse of this process occurs in the shear layer from the opposite of the body. The resulting structure of the wake downstream of the vortex formation region is examined in § 3.3.

Power spectral density of the velocity is used to measure the effect of forcing on the spectral characteristics and structure of the wake. The power spectra at  $\{x, y\} = \{4.5d, 0.8d\}$  for  $\{Re_d = 2500; R = 0, 3.1 \text{ and } 3.9\}$  are presented in figures 14(a) and 14(b), respectively. Without forcing, the power spectrum is dominated by a vortex shedding frequency peak at  $f_v d/u_\infty = \widehat{St}_v = 0.25$ . This value of  $\widehat{St}_v$  is comparable with that measured by Bearman (1965) and Petrusma & Gai (1996) for similar BTE body geometries. Clearly the vortex shedding is attenuated in the forcing cases, but also importantly,  $\widehat{St}_v$  is constant along the span. Interestingly, the power at most frequencies other than  $\widehat{St}_v$  is increased by forcing in the  $R = 3.9$  case. This implies that the break-up of the vortex street in that case also generated a series of smaller-scale structures in the wake, which cascade to even smaller scales. The main difference that is evident

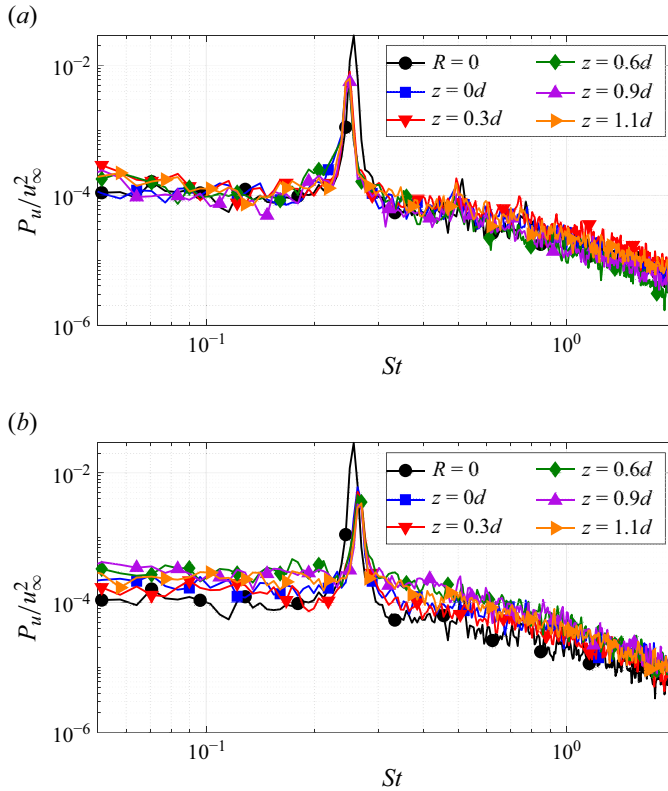


Figure 14. Power spectral density of the velocity, measured along the span at  $\{x = 4.5d, y = -0.8d\}$  at  $Re_d = 2500$  for (a)  $R = 3.1$  and (b)  $R = 3.9$ . Here  $z = 0$  corresponds to the jet-centreline plane.

from the power spectra between the  $R = 3.1$  and  $R = 3.9$  cases at  $Re_d = 2500$  is that the shedding frequency increases to  $\widehat{St}_v \approx 0.26$  for  $R = 3.9$ . Additionally, it is found that further increases to  $R$  drive even higher  $\widehat{St}_v$  and it does not appear to plateau at least up to  $R = 5$ , although these results are not presented in this paper for conciseness. An increase in  $\widehat{St}_v$  is considered undesirable for drag reduction in the present context because it implies that the rate of circulation entering the wake rises.

A spanwise constant  $\widehat{St}_v$  has also been reported in some other distributed forcing studies with different types of spanwise perturbations, such as Park *et al.* (2006) with a series of tabs on a BTE-profiled body, Dobre *et al.* (2006) for a wavy upstream face on a square cylinder and Lam *et al.* (2004) for a wavy cylinder. However, many other distributed forcing studies including Tombazis & Bearman (1997), Bearman & Owen (1998), Bhattacharya & Gregory (2018) and Ling & Zhao (2009) have measured two  $\widehat{St}_v$ . Spanwise  $\widehat{St}_v$  variations cause the phase difference between two locations in the wake to change over time. When the phase difference is small, the vortices can bend along the span but when the difference approaches  $180^\circ$ , the vortex shedding desynchronises along the span and the vortices break. This behaviour was referred to as vortex dislocations by Williamson (1992), and results in a redistribution of the vorticity in the wake. The three-dimensional structure of dislocations is driven by the fact that over several shedding cycles, the out-of-phase von Kármán vortices must reconnect with the upstream and downstream shed vortex cycles from neighbouring cell(s) of different  $\widehat{St}_v$ . For the current forcing

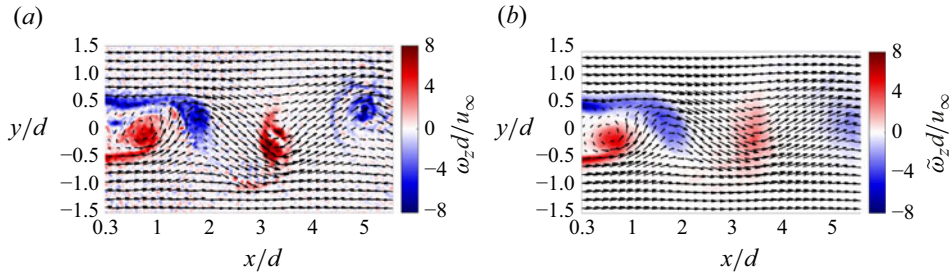


Figure 15. Vorticity field with velocity vectors in the streamwise plane without forcing at  $Re_d = 2500$ . (a) Sample instantaneous field. (b) Phase-averaged field with respect to the vortex shedding.

methodology, the spanwise constancy of  $\widehat{St}_v$  without low-frequency beating suggests a different wake structure from these studies. The work of Kim & Choi (2005) suggests that the reason for the inconsistency in the number of shedding frequencies among different studies may be due to the spanwise wavelength of the flow perturbation. They identified  $\lambda_z = 5d$  as a critical point below which  $\widehat{St}_v$  was constant along the span and above which the wake started to exhibit two shedding frequencies. The forcing wavelength of  $2.4d$  adopted in the present study falls into the low-wavelength regime, so a constant  $\widehat{St}_v$  is consistent with most other studies in this regime. Naghib-Lahouti *et al.* (2015) is a notable outlier reporting different  $\widehat{St}_v$  for  $\lambda_z = 2.4d$ ; however, their  $\widehat{St}_v$  values were measured indirectly from the convective velocity and spatial separation of the von Kármán vortices, which may have introduced errors.

Measurements of the wake in the streamwise  $\{x, y\}$  planes at  $Re_d = 2500$  are used to directly examine the separated shear layers and the vortex street. A representative instantaneous velocity/vorticity field without forcing is shown in figure 15(a). It exhibits the characteristic interaction of the separated shear layers and the resulting vortex street. The vortex formation length is approximately  $1.5d$ . Hence, the von Kármán vortex in the phase shown at  $x \approx 1d$  is still growing from the lower shear layer and the vortex that originates from the upper shear layer at  $x \approx 2d$  has been pinched off by the fluid drawn from the lower part of the base region across the wake centreline.

The periodic component associated with vortex shedding is isolated by conditionally averaging the velocity field measurements with respect to the shedding phase. For the streamwise planes, the reference for the shedding cycle is obtained using a method based on proper orthogonal decomposition (POD) as detailed by van Oudheusden *et al.* (2005). The snapshots were sorted into 18 phase bins, translating to roughly 85 snapshots per bin. Figure 15(b) plots the velocity/vorticity field for the unforced case averaged at a constant phase that roughly corresponds to that shown in figure 15(a). The basic symmetry of vortex shedding is evident with two rows of spanwise vortices that are  $180^\circ$  out of phase between the  $y > 0$  and  $y < 0$  sides. Because vortex shedding is the dominant feature of the wake in the absence of forcing, the instantaneous and phase-averaged fields appear very similar.

The results for  $R = 3.1$  at  $Re_d = 2500$  are examined in the streamwise plane because at this forcing amplitude, the jet vortical structures penetrate approximately up the edges of the boundary layers. This provides strong perturbations to the wake without causing the wake to significantly widen. Phase-averaged velocity/vorticity fields for this case in spanwise-separated planes at  $z = \{0.08d, 0.24d, 0.38d, 0.6d \text{ and } 0.82d\}$  are shown in figure 16. Phase-averaging reveals vortex shedding in all the planes with the same basic symmetry as the unforced case. The shedding phases that are displayed are selected to be consistent with the phase shown in figure 15, approximately corresponding to when

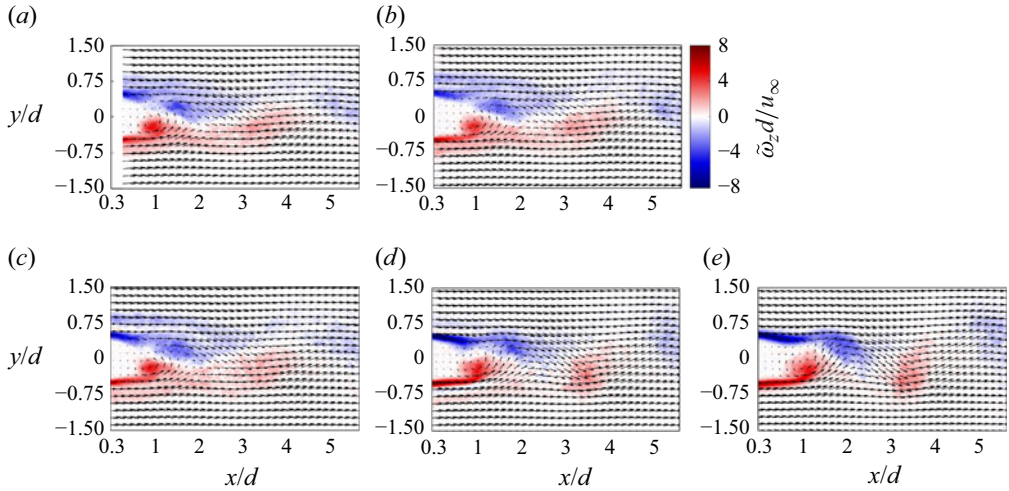


Figure 16. Phase-averaged vorticity fields with velocity vectors in different streamwise planes and forcing for  $R = 3.1$  at  $Re_d = 2500$ : (a)  $z = 0.08d$ , (b)  $z = 0.24d$ , (c)  $z = 0.38d$ , (d)  $z = 0.6d$  and (e)  $z = 0.82d$ .

the negative vortex from the upper side has been fully shed from the body. This phase of the vortex shedding also aligns with that shown in figure 11(b) when the induced streamwise vortices in the separated shear layer reach maximum strength in the lower shear layer at  $x = 1d$ . It is emphasised, though, that this does not imply actual synchronisation between the measurements in the different planes. The vortices on either side of  $y = 0$  have approximately the same strength; however, the overall coherence and strength of the vortex street are reduced, and its three-dimensional nature is apparent from the significantly different distributions of the vorticity across the measurement planes.

In order to quantify the changes in the vortex shedding along the span, the downstream evolution of the circulation contained in the von Kármán vortices,  $\Gamma_v$ , is computed. The vortices are identified here using the  $Q$ -criterion (Hunt, Wray & Moin 1988), where  $Q$  is the second invariant of the velocity-gradient tensor,  $\nabla U$ , for incompressible flows. Mathematically,  $Q = -(\partial u_i / \partial x_k)(\partial u_k / \partial x_i)$ , which for 2-C planar PIV reduces to

$$Q = -\left(\frac{\partial u}{\partial x}\right)^2 - 2\left(\frac{\partial u}{\partial y}\right)\left(\frac{\partial v}{\partial x}\right) - \left(\frac{\partial v}{\partial y}\right)^2, \quad (3.4)$$

if  $w$  and the gradients in  $z$  are neglected. According to the  $Q$ -criterion, vortices exist for  $Q > Q_{thresh}$ , where  $Q_{thresh}$  is theoretically 0. A physical interpretation of this criterion is that vortices are regions where swirling motions make a larger contribution to the vorticity than irrotational shearing motions; however, it does not guarantee that every vortical structure is identified or that every contour of  $Q > 0$  actually corresponds to a vortex. The circulation can be calculated by integrating the spanwise vorticity inside the vortical regions identified for each phase-averaged bin as

$$\frac{\Gamma_v}{u_\infty d} = \iint_S \left(\frac{\tilde{\omega}_z d}{u_\infty}\right) \frac{1}{d^2} dA, \quad (3.5)$$

and the centroids of the vortices are calculated as

$$x_v = \iint_S x \left(\frac{\tilde{\omega}_z d}{u_\infty}\right) \frac{1}{d^2} \left(\frac{\Gamma_v}{u_\infty d}\right)^{-1} dA, \quad (3.6)$$

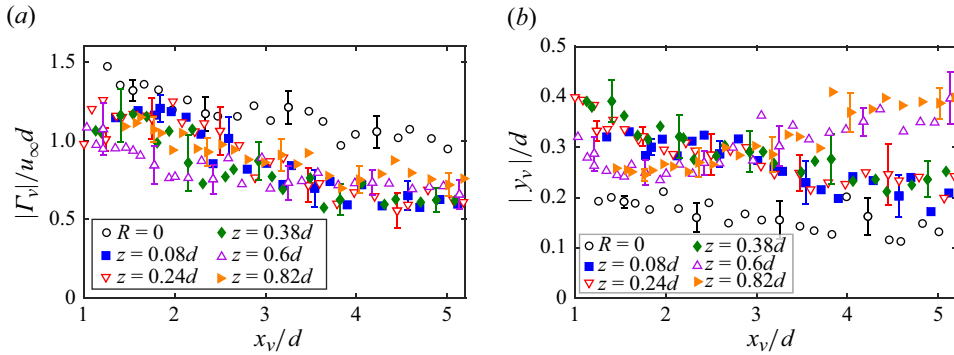


Figure 17. Mean downstream evolution of (a) the circulation contained in the von Kármán vortices and (b) their path in the different streamwise planes that originate from the lower shear layer of the body at  $Re_d = 2500$  without and with forcing at  $R = 3.1$ .

$$y_v = \iint_S y \left( \frac{\tilde{\omega}_z d}{u_\infty} \right) \frac{1}{d^2} \left( \frac{\Gamma_v}{u_\infty d} \right)^{-1} dA. \quad (3.7)$$

In practice, contours at  $Q = 0$  are overly sensitive to measurement noise near the edges of the vortices, and so a slightly positive threshold is preferred to clearly define the vortex boundaries. Thresholds ranging from 0 to 0.5 were tested for  $Qd^2/u_\infty^2$ , and 0.01 was selected for the current datasets. For relatively more positive  $Qd^2/u_\infty^2$  thresholds, the computed circulation values are generally lower because smaller vortical structures are identified. A complication with any  $Q \geq 0$  threshold is that some regions of generally positive  $Q$  may have a few points where  $Q < 0$ . On occasion, this can result in separate  $Q$  regions in close proximity to each other which are clearly part of the same overall vortex. In order to include the entirety of the vortex, the vorticity in the separate regions are added together when any part of their boundaries is within  $0.18d \approx 0.05\lambda_x$  of each other.

The streamwise evolution of the circulation and the paths of the von Kármán vortices are plotted in figure 17 for the unforced and  $R = 3.1$  cases at  $Re = 2500$ . In the absence of forcing, the circulation contained in a vortex just after it is shed is  $\Gamma_v/(u_\infty d) = 1.5$ . The strength of the vortices reaches their maximum at this point and steadily decays downstream. With forcing at  $R = 3.1$ , the circulation of the von Kármán vortices across the span is reduced compared with the unforced case. In the region just downstream of vortex formation ( $1.5d < x < 2d$ ), the circulation of the von Kármán vortices is lowest in the  $z = 0.6d$  plane. This is because a significant fraction of the vorticity entering the wake in the  $z = 0.6d$  plane is not immediately available to be entrained into the von Kármán vortices since it is contained in the outer shear layers. As can be appreciated from figure 16, by  $x \approx 2.5d$ , the outer shear layers are entrained into the von Kármán vortices in the  $z = 0.6d$  plane. This also occurs to an extent in the  $z = 0.38d$  plane; however, in that case, the vortical regions identified by the  $Q$  method encompass both the inner and outer shear layer regions, and so all of this vorticity is summed with the  $Q$  methodology. The von Kármán vortices approach the same strength in all the measurement planes for  $x > 2.5d$ , containing about 65 % of the circulation of the unforced vortices by  $x = 5d$ .

The circulation that forms the vortex street originates from boundary layer separation at the trailing edges of the BTE-profiled body. The rate at which circulation is introduced

into the wake from the separated shear layers,  $d\Gamma_s/dt$ , can be calculated by integrating from the inner edge,  $b$ , to the outer edge,  $s$ , of the shear layer:

$$\frac{d\Gamma_s}{dt} = \int_b^s \bar{u} \bar{\omega}_z dy = \int_b^s \bar{u} \frac{\partial \bar{u}}{\partial y} dy = \frac{1}{2} (\bar{u}_s^2 - \bar{u}_b^2). \tag{3.8}$$

Equation (3.8) approximates  $\partial \bar{v} / \partial x = 0$ , which should be valid for boundary layer flows and around the separation points. Furthermore, it is convenient to assume  $\bar{u}_b = 0$  because the fluid near the trailing edges inside the recirculation region is essentially stationary. Hence, the rate of circulation entering the wake is effectively determined by the excess velocity at the outer edge of the shear layer,  $\bar{u}_s$ . It is instructive to relate the circulation supply from the shear layers,  $\Gamma_s$ , and the resulting average circulation of the shed vortices. From one side of the body,  $\Gamma_s$  can be estimated from the  $\bar{u}$  profile near the separation point/trailing edge assuming that the flow is steady. Following the methodology of Roshko (1954), this involves integrating (3.8) over a shedding period as

$$\Gamma_s = \int_0^{1/f_v} \frac{d\Gamma_s}{dt} dt = \frac{\bar{u}_s^2}{2f_v}. \tag{3.9}$$

In the unforced  $Re_d = 2500$  case,  $\hat{St}_v = 0.25$  and  $\bar{u}_s = 1.125u_\infty$  at  $x = 0.2d$  (see figure 10), so the normalised circulation supply during a shedding cycle is  $\Gamma_s / (u_\infty d) \approx 2.5$ . For the  $\{Re_d = 2500, R = 3.1\}$  case, the separated shear layers asymptotically approach the free stream far enough away from the body, but also exhibit an overshoot (figure 10). In the region between the jets,  $\bar{u}_s = 1.11u_\infty$  and for the profiles closer to the jet centreline,  $\bar{u}_s = 1.1u_\infty$ . Hence, the nominal supply of circulation in the  $\{Re_d = 2500, R = 3.1\}$  case is  $\Gamma_s / (u_\infty d) \approx 2.45$  – about the same as without forcing.

A simple model that relates the circulation in the wake to the separated shear layers is  $\Gamma_s = \Gamma_v + \Gamma_{\mathcal{R}}$ , where  $\Gamma_{\mathcal{R}}$  represents the circulation that is cancelled within the recirculation region. Partial cancellation of the circulation supply from a separated shear layer occurs due to its mixing with opposite-sign vorticity from the shear layer on the other side of the body. This is the main way that vorticity is usually lost in the near wake. For the unforced  $Re_d = 2500$  case,  $\Gamma_s / (u_\infty d) = 2.5$  and  $\Gamma_v / (u_\infty d) = 1.5$ . This implies that in the absence of forcing  $\Gamma_{\mathcal{R}} / (u_\infty d) \approx 1$ , i.e. about 60 % of the circulation survives the vortex formation process and 40 % is cancelled in the recirculation region. This ratio is similar to that reported in other studies of bluff bodies, such as Cantwell & Coles (1983). For the  $R = 3.1$  forcing case,  $\Gamma_v / (u_\infty d)$  appears to settle at approximately  $(0.3-0.4)u_\infty d$  lower than the unforced case in the measured planes. Because the distance that the vortices are shed from the body is similar in the unforced and  $R = 3.1$  cases at  $Re_d = 2500$ , it is reasonable to assume that a similar amount of vorticity is cancelled in the formation region as in the unforced case, i.e.  $\Gamma_{\mathcal{R}} / (u_\infty d) \approx 1$ . Hence, this implies that about  $(0.3-0.4)u_\infty d$  of the total circulation is missing, which is suspected to correspond to the partial diversion of the spanwise von Kármán vortices into streamwise-oriented loops.

An indication of the three-dimensional structure of the vortex street can be obtained from the path of the spanwise vortices in the different planes as plotted in figure 17(b). Without forcing at  $Re_d = 2500$ , the average path of the vortex street is roughly a straight line at about  $0.15d$  away from the wake centreline. In all of the measured planes of the  $\{Re_d = 2500, R = 3.1\}$  case, the von Kármán vortices are initially shed farther away from the wake centreline and take much different paths downstream. In the  $z \leq 0.24d$  planes, the centroids of the vortices start at  $y \approx 0.4$  and gradually advance towards the wake centreline, such that by  $x = 5d$ , they approach  $y = 0.25d$ . However, in the  $z \geq 0.6d$  planes, the centroids of the vortices move in the opposite direction, away from the wake centreline,

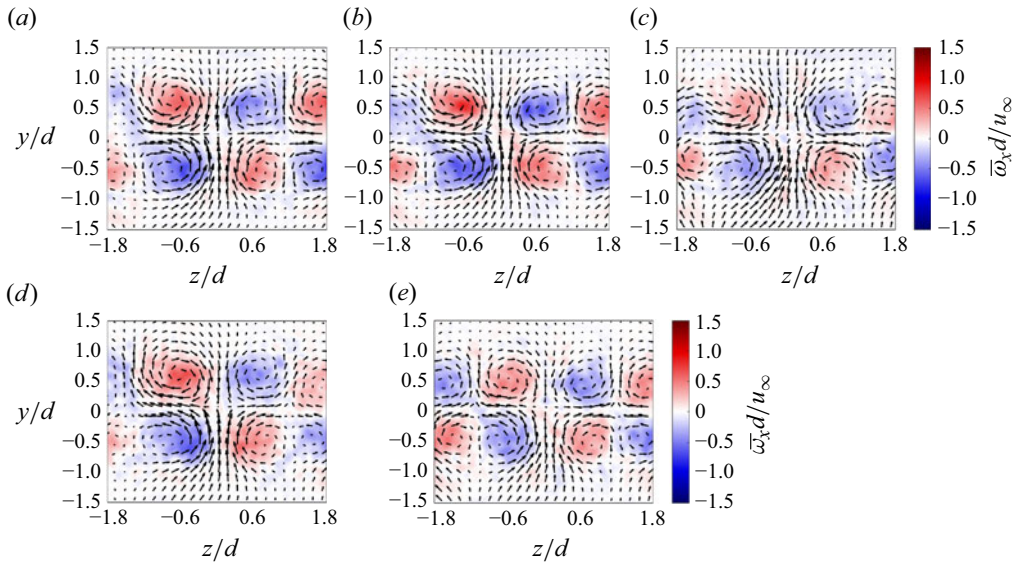


Figure 18. Mean streamwise vorticity field with  $(v, w)$  vectors in the cross-plane at  $x = 4d$  with forcing for (a)  $\{Re_d = 2500, R = 2.7\}$ , (b)  $\{Re_d = 2500, R = 3.1\}$ , (c)  $\{Re_d = 2500, R = 3.9\}$ , (d)  $\{Re_d = 5000, R = 1.9\}$  and (e)  $\{Re_d = 5000, R = 2.5\}$ .

to just below  $|y| = 0.4d$  at the edge of the measurement window. Therefore, despite the similar strength of the von Kármán vortices across the span for  $x \geq 2.5d$ , the cores of the shed vortices exhibit wavy undulations along the spanwise direction in an average sense in response to the imposed forcing disturbances.

### 3.3. Wake three-dimensional structure and the forcing amplitude

The three-dimensional structure of the forced wake can be directly examined using the cross-sectional view from the cross-plane at  $x = 4d$ . The spatial distribution of the mean streamwise vorticity and the velocity with forcing at  $\{Re_d = 2500; R = 2.7, 3.1 \text{ and } 3.9\}$  and  $\{Re_d = 5000; R = 1.9 \text{ and } 2.5\}$  is shown in figure 18. The general symmetry is the same for all these cases, with a pattern of alternating positive and negative streamwise vorticity along the span that is symmetric about the  $y = 0$  and  $z = 0$  planes, forming four vortex concentrations per forcing wavelength. The  $-\omega_x$  vortices are in the  $\{+z, +y\}$  and  $\{-z, -y\}$  quadrants with respect to the jet slot centred at  $z = 0$ , and vice versa for the other quadrants. This matches the sense of rotation of the vortices at  $x = 1d$  in the  $|y| < 0.45$  region (see figure 8), indicating that the organisation enforced on the vortex street during its initial development is maintained downstream. There is no signature of the edge vortices emitted by the actuators at  $x = 4d$ , presumably because those vorticity concentrations are entrained into the overall vortex street or dissipated. Notably, the strength of the streamwise vortices at  $x = 4d$  declines from  $R = 3.1$  to  $R = 3.9$  at  $Re_d = 2500$  and from  $R = 1.9$  to  $R = 2.5$  at  $Re_d = 5000$ . This aligns with the change in the jet–boundary layer interaction at these  $Re_d$  previously observed at  $x = 1d$  in figure 8. Furthermore, the vortices in the  $\{Re_d = 2500, R = 2.7\}$  case are relatively closer in strength to those in the  $\{Re_d = 5000, R = 1.9\}$  case than  $\{Re_d = 5000, R = 2.5\}$ . This is another indication that  $R$  is not ideal for comparing across different  $Re_d$  with the present methodology.

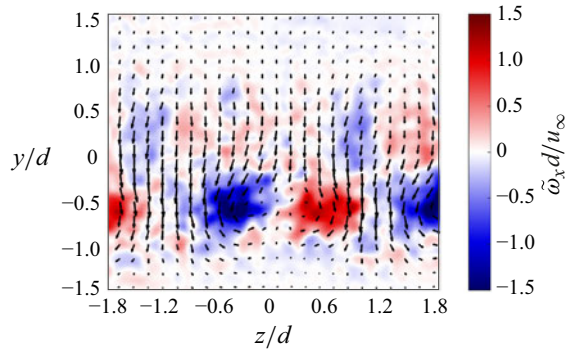


Figure 19. Phase-averaged streamwise vorticity field with  $(v, w)$  vectors at a phase where it is maximised in the  $y < 0$  half of the cross-plane at  $x = 4d$  with forcing at an amplitude of  $R = 2.7$  at  $Re_d = 2500$ .

The streamwise vortices at  $x = 4d$  are reflective of the spanwise phase variations in the vortex shedding. To examine the connection of these vortices to the vortex shedding, the measurements are phase-averaged with respect to the shedding cycle. The streamwise plane measurements indicate that for forcing amplitudes where the jets do not penetrate beyond the boundary layer,  $x = 4d$  is far enough downstream that the vortex street has established a periodic structure, whereas for the higher-forcing-amplitude cases, the structure may not yet be fully established. The cross-plane measurements are phase-averaged directly with respect to the velocity near the outer edge of the shed vortices close to the free stream at  $\{x, y\} = \{4d, 1.25d\}$  using the methodology described in [Appendix A](#). Each case was subdivided into 16 phase bins, resulting in approximately 65 snapshots per bin.

Phase-averaging shows that the counter-rotating streamwise vortex pairs alternate between both sides of the wake over a shedding cycle at  $x = 4d$ . [Figure 19](#) captures the phase when the streamwise vorticity is at its greatest in the  $y < 0$  half for  $R = 2.7$  at  $Re_d = 2500$ . This case is emphasised in this section because it most clearly demonstrates the organisation of the induced three-dimensional wake structure, but a similar organisation is evident in the  $\{Re_d = 2500, R = 3.1\}$  case and it also appears in the  $Re_d = 5000$  cases. In spite of the jets being active from both sides of the body throughout the entirety of the shedding cycle, almost no streamwise vorticity is evident in the  $y > 0$  half at this phase. Half a shedding period later, the situation flips and streamwise vorticity is maximised in the  $y > 0$  half of the wake, except that the streamwise vortices have opposite sense of rotation. The fact that the streamwise vorticity coherently varies over the shedding cycle indicates that symmetric perturbations to the wake (about  $y = 0$ ) still result in an anti-symmetric wake structure due to presence of vortex shedding. It is consistent with the streamwise vortices at  $x = 4d$  being loops that originate from the von Kármán vortices. The phases where the streamwise vorticity is maximised are expected to occur when the vortex legs are most normal to the cross-plane, and should also correspond to when the  $\tilde{\omega}_y$  components of the loops are at their weakest. The comparable magnitude of  $\tilde{\omega}_x$  in the cross-plane to  $\tilde{\omega}_z$  of the von Kármán vortices in the streamwise plane underscores that these loops are a deformation of the von Kármán vortices. The spanwise separation between the positive and negative streamwise vortex pairs is approximately  $1.2d$ . Therefore, the spanwise wavelength of the vortex loops matches the  $\lambda_z = 2.4d$  of the actuator spacing.

The vortical symmetry with the present distributed forcing methodology is the same across all the forcing amplitudes and  $Re_d$  investigated. It is similar to that reported by

Park *et al.* (2006) for distributed forcing with tabs, and is consistent with the mean vorticity fields shown in the study of Zhang & Lee (2005), for example. Although Zhang & Lee (2005) did not directly investigate the shedding phase-dependent variations, it is reasonable to infer vortex looping based on their presented results. The streamwise vorticity fields resulting from the present forcing methodology are also superficially similar to the fields in the study of Bhattacharya & Gregory (2018). However, they reported that the streamwise vorticity distribution was independent of the shedding phase and did not alternate across the  $y = 0$  plane. This suggests that the streamwise-induced vortices in the work of Bhattacharya & Gregory (2018) were not loops of the von Kármán vortices. Additionally, Bhattacharya & Gregory (2018) found that the streamwise vortices could change their symmetry depending on the forcing amplitude and spanwise wavelength. This highlights that different three-dimensional forcing schemes can also be beneficial for the drag reduction of two-dimensional bluff bodies. However, it is clear that the imposition of streamwise vorticity in the wake through spanwise-induced variations of the streamwise velocity is a common feature of different three-dimensional control strategies and is closely connected to the underlying mechanism. In discussing spanwise wavy wakes from a linear stability perspective, Hwang, Kim & Choi (2013) found that von Kármán vortex shedding was stabilised due to sinusoidal base flow perturbations along the span. They argued that the stabilisation mechanism in their study proceeded in two steps. First, their imposed spanwise variation in the streamwise velocity field tilted the von Kármán vortices into the streamwise direction, resulting in the generation of streamwise vorticity. Next, the streamwise vortex loops interacted with the spanwise von Kármán vortices due to the spanwise shear in the base flow to attenuate the vortex shedding. This is essentially in line with the present experimental observations even though the perturbation to the flow is not purely sinusoidal along the span with the synthetic jet array and some streamwise vorticity is directly introduced into the wake by the actuators.

The phase-averaged structure of the vortex street in unforced and forced conditions can be visualised in three dimensions by stacking the two-dimensional phase-averaged stereo cross-planes. The phase dimension is converted to the  $x$  spatial dimension using the  $\lambda_x \approx 3.5d$  of the vortex street that is measured in the streamwise planes. This provides a three-dimensional approximation of the wake structure. Isosurfaces of the phase-averaged vorticity for the unforced and  $R = 2.7$  cases at  $Re_d = 2500$  are given in figure 20. The vorticity is coloured by the vector components at a constant level of  $\omega_i d / u_\infty = 0.3$ . The spanwise components of the von Kármán vortices are coloured red and blue for positive and negative concentrations, respectively, which show the characteristic anti-symmetric structure of vortex shedding. The  $|\omega_x|$  component is green and  $|\omega_y|$  is purple. In the unforced case, the  $|\omega_x|$  and  $|\omega_y|$  surfaces do not form coherent structures in a phase-averaged sense. These components are connected to construct vortex loops in the  $R = 2.7$  case that repeat along the span with a wavelength matching the spacing of the actuators. The loops exist in the braid region of the vortex street where the strain rate of the flow is high, outside of the cores of the von Kármán vortices. For convenience, the loops may be referred to as streamwise vortices, but as they wrap around a von Kármán vortex, the loops reorient to be principally in the  $y$  direction.

An illustration of the vortical structure is given in figure 21. The principal direction of the von Kármán vortices is spanwise in the illustration, but loops are pulled out of each von Kármán vortex in the upstream direction symmetrically about the jet centreline planes ( $z = 0$ ) and wrap around the neighbouring upstream von Kármán vortex shed from the opposite side of the body. The sense of rotation of the streamwise vortices is determined by that of the von Kármán vortices. The vortex legs seen in the  $y > 0$  half of the cross-plane originate from the  $-\omega_z$  von Kármán vortices, and vice versa for the vortex legs in

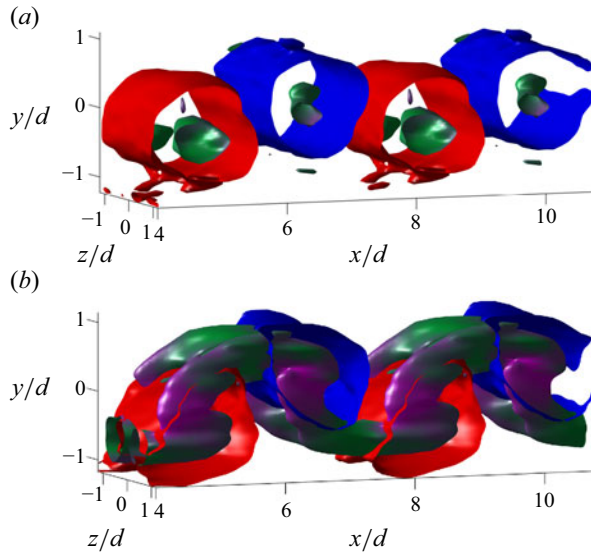


Figure 20. Phase-averaged vorticity isosurfaces, coloured by vector component at a constant level of  $\omega_i d/u_\infty = 0.3$  for  $Re_d = 2500$  cases: unforced and (b)  $R = 2.7$ . Red and blue surfaces correspond to positive and negative  $\omega_z$ , respectively: Green is  $\omega_x$  and purple is  $\omega_y$ , which are joined together to form unified surfaces.

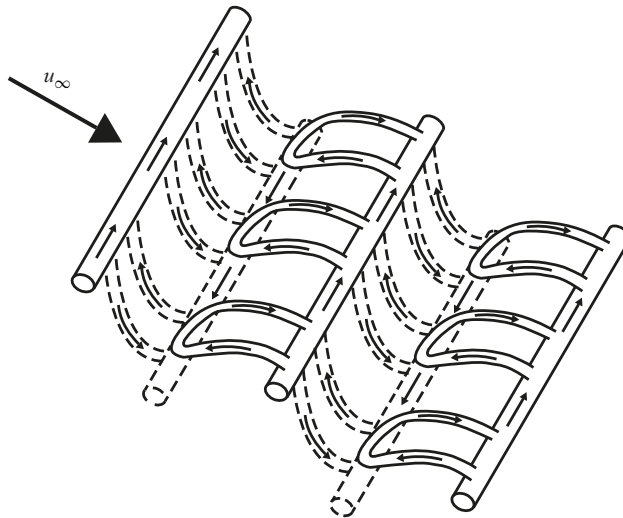


Figure 21. Vortical structure of the wake with distributed forcing. Streamwise vortex loops are pulled out of the spanwise-oriented von Kármán vortices. This forms a line of vorticity along the streamwise direction that switches direction once per shedding wavelength.

the  $y < 0$  half. A vortex leg that is pulled out of a von Kármán vortex in the upstream direction at a given  $z$  location will have the opposite sense of rotation to the streamwise vortex leg that is pulled in the exact same direction from a von Kármán vortex shed from the opposite side of the body because the spanwise sense of rotation of the von Kármán vortices switches. Over a shedding period, the sense of rotation of a streamwise vortex at a given  $z$  location therefore switches sign once. Equivalently, it forms a line of streamwise vorticity along the  $x$  direction that periodically alternates between positive and negative

once during each shedding wavelength. Hence, the vortex loops link together von Kármán vortices that rotate in opposite directions, forming a closed structure that repeats every half shedding wavelength.

The type of symmetry in the forced wake is also exhibited in some other natural vortical flows. For example, it is reminiscent of the three-dimensional structure predicted by Ashurst & Meiburg (1988) in a temporally evolving plane shear layer subject to a Kelvin–Helmholtz instability. This pattern was later simulated and experimentally produced by Lasheras & Choi (1988), Meiburg & Lasheras (1988) and Lasheras & Meiburg (1990) for shear layers, as well as the wake of a flat plate at  $Re_d \approx 100$ . Lasheras & Choi (1988) excited a shear layer with small sinusoidal spanwise perturbations and observed the development of three-dimensionality in the resulting flow. They found that the Kelvin–Helmholtz instability developed first, producing spanwise vortices. Farther downstream, the perturbed vorticity on the braids of the spanwise vortices was stretched in the streamwise direction to form vortex loops. These streamwise vortices then induced waviness along the cores of the spanwise vortices through nonlinear interactions. Meiburg & Lasheras (1988) observed the tilting of spanwise von Kármán vortices in the wake of a flat plate at  $Re_d \approx 100$  with spanwise perturbations. The vortical symmetry observed in these studies as well as the present work is also essentially the same as the self-sustaining mode A secondary instability in wakes described by, for example, Williamson (1996).

Poncet *et al.* (2008) argued for a connection between optimal drag reduction and the natural secondary instabilities of modes A and B because their numerical work identified that drag minimums occurred for spanwise perturbations near the wavelengths of these instabilities. Similar arguments have been put forth by Dobre *et al.* (2006), Bhattacharya & Gregory (2015) and Naghib-Lahouti *et al.* (2015). In the present study, the arrangement of the vortex loops in the forced wake arises because the actuators are located symmetrically about both sides of the BTE body. This keeps the induced loops from the upper and lower sides of the body approximately in line downstream of the jets. The fact that this arrangement aligns with the mode A vortices could be construed as supporting the hypothesis of Poncet *et al.* (2008). However, the mode A instability is typically associated with the early stages of the wake transition regime ( $Re_d < 1000$ ) and not in the turbulent wake regime of the present work. Moreover, the spanwise wavelength of the mode A vortices is about  $4d$  (Ryan, Thompson & Hourigan 2005). The fact that this is much greater than the wavelength of the forcing indicates that, at the very least, matching the mode A instability is not required for distributed forcing.

The other secondary wake instability for this BTE body geometry, mode B, is not a reorientation of the von Kármán vortices at all. The mode B instability is speculated to develop in the braid region of the von Kármán vortices (Williamson 1996) or to be a three-dimensional instability of the separated shear layers (Brede, Eckelmann & Rockwell 1996). This mode persists throughout the turbulent wake regime, but its characteristic spanwise wavelength is approximately  $1d$  and its vortical symmetry is different from that induced in the current investigation (Gibeau *et al.* 2018). For the mode A, the vortices form lines of the same-sign streamwise vorticity along  $x$  instead of alternating every half-shedding cycle. It may be possible to induce this type of symmetry in the streamwise vorticity field by staggering the actuators along the span by  $\lambda_z/2$  between the upper and lower sides of the BTE body. However, the vertical symmetry of the wake would likely be lost with a staggered arrangement of the actuators, i.e. the strength of the von Kármán vortices would be different from both sides of the body at a given  $z$  location, and this is unlike the mode B instability. Therefore, it would be challenging to produce the overall symmetry of the mode B even with a staggered arrangement of actuators at a spanwise wavelength of  $\approx 1d$ . The spanwise wavelength of the present forcing configuration matches that of

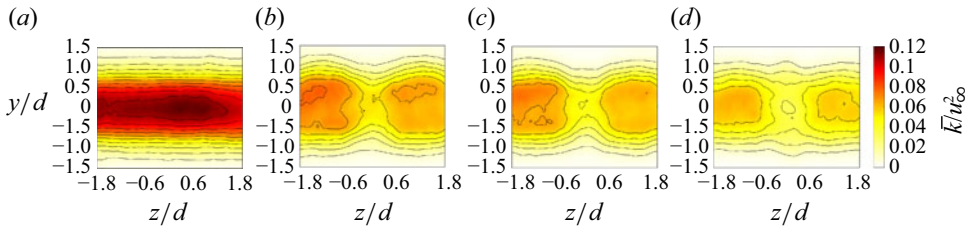


Figure 22. Distribution of  $\bar{k}$  in the cross-plane at  $x = 4d$  when  $Re_d = 2500$ : (a) without forcing, (b)  $R = 2.7$ , (c)  $R = 3.1$  and (d)  $R = 3.9$ .

Naghib-Lahouti *et al.* (2015), who perturbed the wake at  $\lambda_z = 2.4d$  in order to match the wavelength of a mode B' instability. However, recent work by Gibeau *et al.* (2018) has cast significant doubt on whether a mode B' exists at all. Moreover, the overall topology of the mode B' would match the mode B if it does exist, with the streamwise vortices maintaining the same sense of rotation along  $x$  at a given  $z$  location (Naghib-Lahouti *et al.* 2014). Hence, the vortical structures introduced by the present forcing arrangement would not be expected to align with the mode B' either. It is therefore improbable that distributed forcing depends on interactions with secondary instabilities.

Figure 22 shows the distribution of  $\bar{k} = 0.5(\overline{u'u'} + \overline{v'v'} + \overline{w'w'})$  in the cross-plane without and with forcing at  $\{Re_d = 2500; R = 0, 2.7, 3.1 \text{ and } 3.9\}$ . As previously indicated in figure 14, the magnitude of the velocity fluctuations in the near wake is largely reflective of the strength of the vortex shedding. The total magnitude of the fluctuations is generally the highest along the wake centreline ( $y = 0$ ) because it experiences the full extent of the cross-stream velocity variations induced by the von Kármán vortices shed from both sides of the body, and the  $v$  fluctuations are typically stronger than the  $u$  fluctuations in this region. Forcing causes  $\bar{k}$  to decline throughout the cross-plane, primarily because of the attenuation of the vortex shedding. As a result of the spanwise-periodic nature of this forcing strategy,  $\bar{k}$  is noticeably lower closer to the jet centreline at  $z = 0$  compared with that between the jets.

The streamwise vortices in the wake induced by the synthetic jet array resemble those measured for a wavy cylinder by Zhang & Lee (2005). The sense of rotation of the vortices is such that the spanwise regions downstream of the jet centrelines are analogous to the cylinder saddles, and the regions between jet slots correspond to the nodes. In essence, the synthetic jet forcing creates similar spanwise velocity gradients in the separated shear layers to those that naturally occur for bodies with wavy geometries in order to achieve a similar effect on the vortex shedding. The situation is also analogous because in the low- $\lambda_z$  regime of a wavy cylinder, Zhang & Lee (2005) found that the minimum  $\bar{k}$  in the wake downstream of the vortex formation region occurs in the saddle plane, and with the synthetic jet array,  $\bar{k}$  is minimised along the jet centreline plane.

The distribution of  $\overline{\omega_z}$  and  $\bar{k}$  with the synthetic jet forcing scheme is also similar to that measured by Bhattacharya & Gregory (2018) in their high amplitude forcing and  $\lambda_z \geq 4d$  regime for distributed plasma actuators on a cylinder; however, they argued that the streamwise vortices did not alternate with the vortex shedding cycle. Synthetic jets were used as the actuator for distributed forcing on a cylinder by Cui, Feng & Liu (2020), who reported introducing streamwise vorticity into the wake, but there was not a clear symmetry of the wake vortical structures downstream of the vortex formation length, perhaps because the vortex shedding was more significantly disorganised than in the

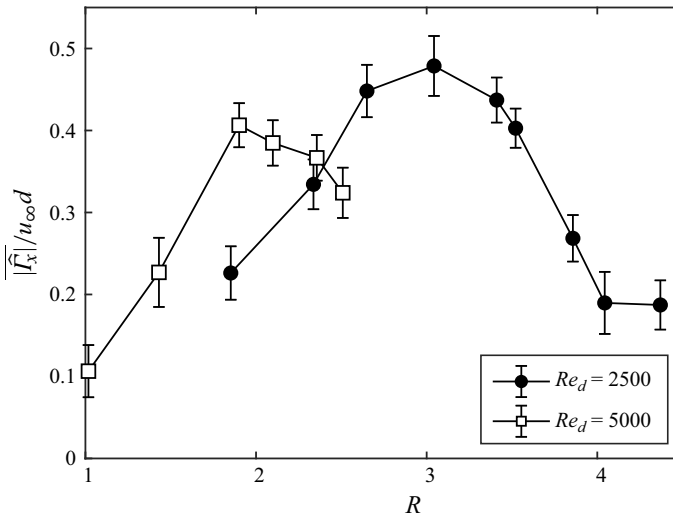


Figure 23. Peak phase-averaged streamwise circulation of the von Kármán vortex loops during a vortex shedding cycle as a function of  $R$  for  $Re_d = 2500$  and  $5000$ .

present case. Therefore, the work of neither Bhattacharya & Gregory (2018) nor Cui *et al.* (2020) is directly comparable with the present forcing methodology.

The circulation of the streamwise vortices is computed to test whether it can account for the missing circulation in the spanwise von Kármán vortices from the streamwise-plane PIV measurements. The PIV cross-plane at  $x = 4d$  is divided into quadrants bounding  $0 \leq |z| \leq 1.2d$  and  $0 \leq |y| \leq 1.05d$  which encompass each leg of the streamwise vortices. The vortices in each quadrant are tracked in a phase-averaged manner to measure how the streamwise circulation changes over the vortex shedding cycle. The vorticity inside each of the legs is integrated to compute the circulation for each phase bin,  $\phi_v$ , as

$$|\Gamma_x(\phi_v)| = \iint_{\mathcal{S}} |\tilde{\omega}_x(\phi_v)| dA = \sum_i \sum_{\kappa} |\tilde{\omega}_x(\phi_v)| \Delta y \Delta x, \quad (3.10)$$

where  $\mathcal{S}$  is the surface boundary,  $i$  and  $\kappa$  are indices and  $\Delta x = \Delta y = 0.039d$ . The integration bounds are set by lines of constant vorticity at  $|0.15u_{\infty}d|$  to reject noisy data near the vortex edges. The two vortices located in the  $y > 0$  half, as well as the vortices in the  $y < 0$  half, form pairs consistent with a vortex loop structure. The phase with maximum circulation is typically the same for the vortices in a pair, and variations in the circulation are approximately  $180^\circ$  out of phase between the loops located in the  $y > 0$  and  $y < 0$  halves of the wake. The average of the peak circulations in all four quadrants is given by  $|\widehat{\Gamma}_x|$ , where

$$|\widehat{\Gamma}_x| = \frac{1}{4} (|\widehat{\Gamma}_x|_{Upper\ left} + |\widehat{\Gamma}_x|_{Upper\ right} + |\widehat{\Gamma}_x|_{Lower\ left} + |\widehat{\Gamma}_x|_{Lower\ right}). \quad (3.11)$$

The variation of  $|\widehat{\Gamma}_x|$  with  $R$  at  $Re_d = 2500$  and  $5000$  is summarised in figure 23. It can be seen that  $|\widehat{\Gamma}_x| / (u_{\infty}d)$  increases up to about 0.45 when  $Re_d = 2500$  and 0.4 when  $Re_d = 5000$ . Recalling the discussion in § 3.2,  $|\widehat{\Gamma}_x| / (u_{\infty}d) = 0.45$  is in line with the amount of spanwise circulation hidden from observation in the streamwise planes. This supports the hypothesis that the total circulation entering the wake is similar with and without forcing,

but that about one-third of this circulation is in the streamwise/cross-stream directions in the best-case forcing scenario.

Consistent with the observations from figure 18, figure 23 shows that  $\overline{|\widehat{\Gamma}_x|}/(u_\infty d)$  is maximised at  $R = 3.1$  when  $Re_d = 2500$  and at  $R = 1.9$  when  $Re_d = 5000$ . An indication of how the scaling of the forcing amplitude should be modified to achieve better collapse with  $Re_d$  is that the  $\overline{|\widehat{\Gamma}_x|}$  peak of the  $Re_d = 2500$  case occurs at about the same forcing amplitude that a significant amount of positive vorticity starts to appear at the upstream side of the jet slot, which is associated with the jet structure changing to a type that is more penetrating (see figure 6). At both  $Re_d = 2500$  and  $5000$ , this critical forcing amplitude aligns with when the jet vortices penetrate just up to the edge of the boundary layer, suggesting that the forcing effectiveness is more closely linked to the jet penetration. The wall-normal penetration rate of a jet in a cross-flow is related to the momentum flux introduced by the jet. Using an empirical power law based on  $R^\gamma \mathcal{D}$ , the penetration distance of a continuous jet emitted from a circular orifice is conventionally described as

$$\frac{y_j}{R^\gamma \mathcal{D}} = A \left( \frac{x_j}{R^\gamma \mathcal{D}} \right)^n, \quad (3.12)$$

where  $A$ ,  $n$  and  $\gamma$  are constants,  $y_j$  is the wall-normal jet penetration distance relative to the model surface and  $x_j$  is the streamwise distance from the jet origin (Mahesh 2013; Berk *et al.* 2018). The scaling of synthetic jet penetration is complicated by their unsteady nature. Assuming that the synthetic jet formation criterion is met and that the vortices generated by a synthetic jet are not re-ingested into their cavities, the circulation initially emitted into a flow comes from the developed vortex rings. Using a boundary layer approximation, the instantaneous rate of circulation generation,  $\Gamma_j$ , during the formation of a vortex ring from a synthetic jet slot is

$$\frac{d\Gamma_j(t)}{dt} \approx \frac{\partial u_j(t)}{\partial x} u_j(t) dx \approx \frac{u_j(t)^2}{2}, \quad (3.13)$$

where  $u_j(t)$  is the instantaneous centreline jet velocity (Glezer 1988). The circulation emitted from a synthetic jet varies periodically over the expulsion cycle, and it can be shown in non-dimensional form by integrating (3.13) over the period of an expulsion cycle,  $T_j/2$ , that  $\Gamma_j/(\mathcal{D}u_\infty) \propto R^2/St_j$ , where  $St_j = f_j \mathcal{D}/u_\infty$  (Berk & Ganapathisubramani 2019). Using as a physical basis that the wall-normal velocity of a jet is proportional to the emitted circulation in a vortex ring, Berk & Ganapathisubramani (2019) argued that synthetic jet penetration should be a function of  $\Gamma_j/(\mathcal{D}u_\infty) \propto R^2/St_j$ . Hence, they proposed scaling the penetration distance as

$$\frac{y_j/d}{(R^2/St_j)^{0.6}} = A \left( \frac{x_j/d}{(R^2/St_j)^{0.6}} \right)^{0.26}. \quad (3.14)$$

It is instructive to examine whether the scaling of Berk & Ganapathisubramani (2019) can model the jet penetration for the various cases in the current work. The primary interest here is  $y_j/d$  when it is close to the trailing edge of the BTE model. If the actual path that the jet takes is not included in the model, then the  $x_j/d$  dependence can be grouped with the  $A$  constant to form  $A^\dagger$ . This results in a final simplification of

$$y_j/d = A^\dagger (R^2/St_j)^{n^\dagger}, \quad (3.15)$$

by rearranging (3.14).

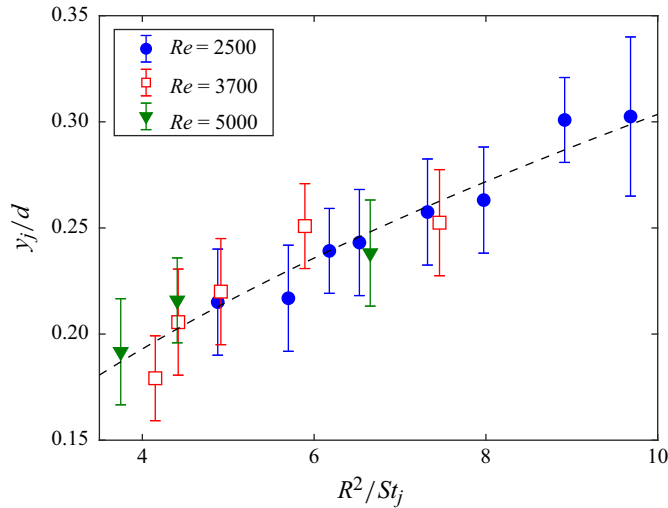


Figure 24. Mean penetration distance,  $y_j/d$ , of the vortical structures generated by forcing, measured at  $x = 0.2d$  and  $0.4d \leq z \leq 0.6d$ , over a range of  $Re_d$  and forcing amplitudes where the vortical structures remain inside the boundary layer. The dashed line shows the best fit through the datapoints:  $y_j/d = 0.1(R^2/St_j)^{0.49}$ .

Shear layer velocity profiles were measured at a fixed streamwise location of  $x = 0.2d$  with HWA to determine  $y_j/d$  for a range of forcing amplitudes that the jet did not penetrate outside the boundary layer at  $Re_d = 2500, 3700$  and  $5000$  (see figure 10 as an example for the  $Re_d = 2500$  and  $R = 3.1$  case). For these forcing amplitudes, the induced edge vortices remain close to the jet slot edges, producing the highest peaks in  $\overline{u'u'}$  in the profiles taken at  $0.4d \leq z \leq 0.6d$ . Therefore,  $y_j/d$  is most appropriately identified from the shear layer profiles in this range. The  $y_j/d$  location of the jet is defined here as the local peak in  $\overline{u'u'}$ , although alternative definitions such as the local minimum in the mean velocity or local maximum in the velocity gradient could have been used (Smith 2002). The  $\overline{u'u'}$  peak is used to define  $y_j/d$  because it was more reliable than the other methods at discriminating between the peak associated with the jet and the peak from the wake shear layer of the BTE body itself. Figure 24 summarises the computed  $y_j/d$  for the different forcing amplitudes measured at  $Re_d = 2500, 3700$  and  $5000$ . The wall-normal jet penetration datapoints follow a trend line that suggests that the model of Berk & Ganapathisubramani (2019) is appropriate for the present forcing methodology. The curve fit is best described as  $y_j/d = (0.1 \pm 0.01)(R^2/St_j)^{0.49 \pm 0.09}$ , where notably this  $n^\dagger$  is consistent with the value of 0.44 obtained by Berk & Ganapathisubramani (2019).

The streamwise circulation of the von Kármán vortex loops is scaled based on the jet penetration height using  $(R^2/St_j)^{0.5}$ , rounding to  $n^\dagger = 0.5$ . Figure 25 shows that  $|\widehat{\Gamma}_x|$  exhibits good correspondence with  $(R^2/St_j)^{0.5}$  for both  $Re_d = 2500$  and  $5000$ . This indicates that  $|\widehat{\Gamma}_x|$  is better expressed as a function of the jet penetration height rather than  $R$  or  $C_\mu$  for the present forcing methodology. Evidently, the effectiveness of the present forcing scheme is more related to how the jet penetrates inside the boundary layer rather than the strength of the jet itself. Because the boundary layer thickness,  $\delta$ , for a given chord length is related to  $Re_d^{-0.5}$ , a jet at the same  $R$  penetrates to a higher  $y_j/\delta$  when  $Re_d$  increases. This helps to explain why the strength of the induced streamwise von Kármán vortex loops for the same  $R$  increases with  $Re_d$ . However, the corresponding decrease in the boundary layer thickness with  $Re_d$  also restricts the maximum strength of the jet that

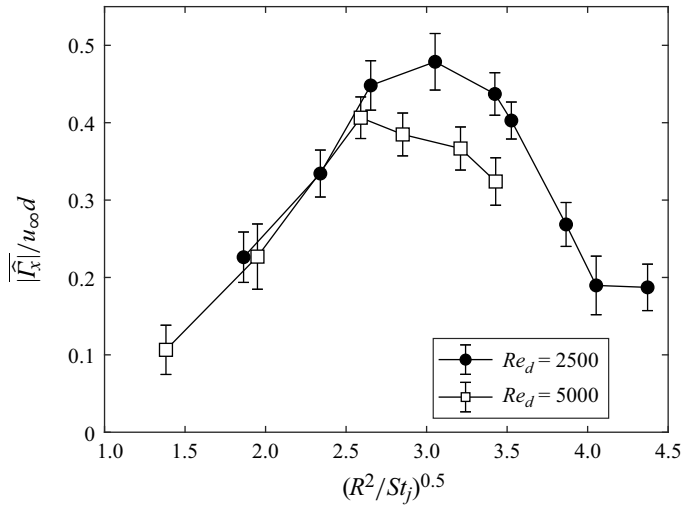


Figure 25. Peak phase-averaged streamwise circulation of the von Kármán vortex loops during a vortex shedding cycle as a function of  $(R^2/St_j)^{0.5}$  for  $Re_d = 2500$  and  $5000$ .

can be attained without penetrating past the boundary layer edge. This limits the ability of the present forcing scheme to redirect the spanwise von Kármán vortices into streamwise vortex loops and points to a lower maximum effectiveness at higher  $Re_d$  for a given BTE body geometry with the present forcing strategy.

### 3.4. Drag

Attenuated vortex shedding is typically associated with reduced drag due to the close connection between the concentration and formation distance of the shed von Kármán vortices, and the resulting mean and fluctuating forces acting on a bluff body. A planar momentum balance is employed with the PIV data to estimate the drag changes as a result of forcing. The main assumptions are that the incoming flow is uniform and steady, the only external force that acts on the control volume is the drag in the  $x$  direction, the flow enters and exits the control volume only along the  $\{y, z\}$  plane boundaries and the pressure in the free stream at the outflow plane is the same as at the inflow plane. Based on these assumptions, the equation for the drag coefficient from the velocity profile at the exit plane,  $S_{out}$ , is derived in Appendix B as

$$c_d = \frac{2}{u_\infty^2} \int_{S_{out}} \left( u_\infty (\bar{u}^2 + \bar{w}^2)^{1/2} - \bar{u}^2 - \overline{u'u'} + \overline{v'v'} \right) d\left(\frac{y}{d}\right). \quad (3.16)$$

For the streamwise 2C-PIV planes, the contribution of the  $w$  term is neglected since it is not measured. The value of  $c_d$  in these planes is computed as a function of  $x$  and plotted in figure 26 for  $Re_d = 2500$ . It can be seen that  $c_d$  declines when moving downstream. The lack of convergence in  $c_d$  is most likely related to the assumption that the pressure at the inflow is the same as the free-stream pressure in the wake when, in actuality, the free-stream pressure is still recovering in the near wake. Hence, the computed  $c_d$  values are inflated. The true  $c_d$  for the present BTE-profiled body is unknown but  $c_d = 0.57$  was measured by Li, Bai & Gao (2015) using force transducers for a BTE-profiled body where  $r_{LE} = d$ , so the true  $c_d$  for the present body is likely similar. The best estimate of  $c_d$  that can be achieved with a momentum balance from the present data is from the downstream edge of the measurement domain at  $x = 5.5d$ . Without measuring further downstream

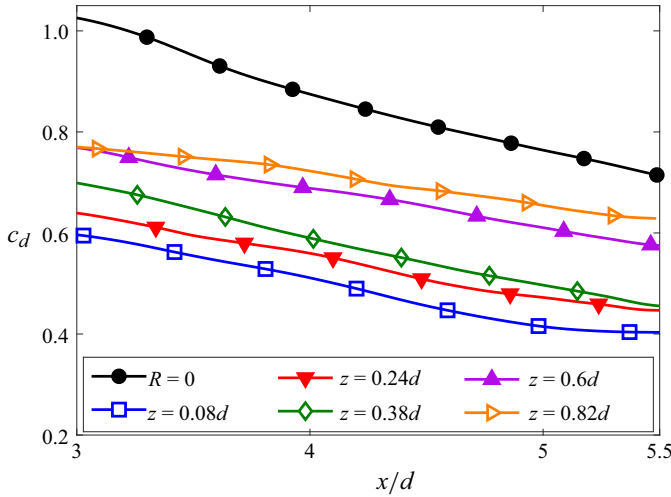


Figure 26. Downstream evolution of  $c_d$  in the unforced  $Re_d = 2500$  case and with forcing at an amplitude of  $R = 3.1$  across the different streamwise PIV planes.

to improve the reliability of the computations, the  $c_d$  values at  $x = 5.5d$  should provide enough information for comparison purposes. In the absence of forcing,  $c_d = 0.71$  at  $x = 5.5d$ . The local  $c_d$  values in all the measured streamwise planes of the  $\{Re_d = 2500, R = 3.1\}$  case are consistently lower than those of the baseline case, highlighting that this forcing condition reduces the drag. As suggested by the spanwise-variable nature of this forcing strategy, the local  $c_d$  changes significantly along the span. The drag is lowest close to the jet centreline due to the greater degree of vortex street attenuation in this plane and gradually increases away from the jet centreline.

The cross-plane data are used to determine the net  $\langle c_d \rangle$  by spanwise averaging over a distance of one forcing wavelength for  $-1.2d < z < 1.2d$ . The measurements in the cross-plane allow for a more complete analysis of  $\langle c_d \rangle$  because of the much better spanwise resolution compared with the spanwise-separated streamwise planes. Additionally, the  $\bar{w}$  term of  $c_d$  in (3.16) can be included using the cross-plane data. For the forcing cases, the  $\bar{w}$  term contributes to at most about 5% of the local  $c_d$  at the  $z$  locations where the forcing induces the strongest  $\bar{w}$  motions. There is a greater bias error in the drag computations made from the cross-plane than from the streamwise planes because the cross-plane is located even closer to the model than the  $x = 5.5d$  point that was available from the streamwise planes. The streamwise-plane data indicate that the  $c_d$  values in the cross-plane at  $x = 4d$  are about 0.1–0.15 higher than they would be if they were measured at  $x = 5.5d$ . Nevertheless, the trends in how  $\langle c_d \rangle$  varies between the forcing cases are not expected to change much if the cross-plane was located further downstream. Because the relative  $\langle c_d \rangle$  trends are of more interest than the absolute values for this study, this inflation from the cross-plane is an acceptable compromise for the greatly improved spanwise resolution.

Considering the bias of the computed  $c_d$  values, the results are summarised as ratios relative to the unforced case,  $\langle c_d \rangle / \langle c_{d,0} \rangle$ , in figure 27. It presents  $\langle c_d \rangle / \langle c_{d,0} \rangle$  as a function of  $(R^2/St_j)^{0.5}$  for the  $Re_d = 2500$  and 5000 cases as the red dashed lines. The drag exhibits a minimum at both  $Re_d$  that is about 25% lower than that of the respective unforced cases. As understood by von Kármán (1912), the pressure drag of a bluff body is directly related to the strength of its vortex street. Physically, the greater the concentration of the shed vortices, the larger the kinetic energy of the wake. Because the energy to create the

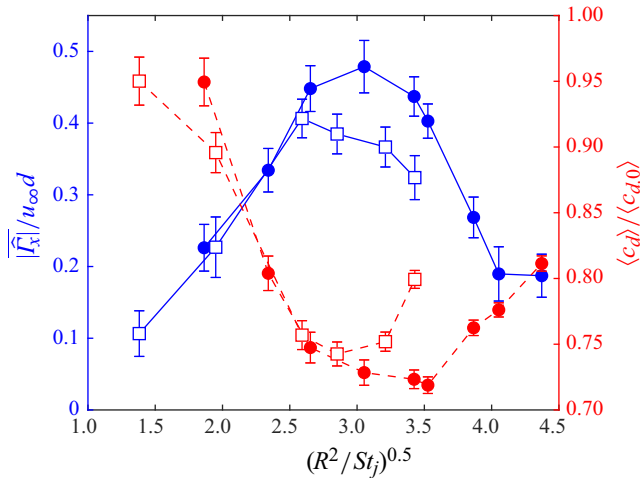


Figure 27. Spanwise-averaged drag ratio,  $\langle c_d \rangle / \langle c_{d,0} \rangle$  (red), plotted alongside the streamwise circulation,  $|\widehat{\Gamma}_x|$ , of the von Kármán vortex loops (blue) as a function of forcing amplitude. The forcing amplitude is scaled based on the jet penetration distance,  $(R^2/St_j)^{0.5}$ . Here  $Re_d = 2500$  and  $5000$  are represented by the circle and square datapoints, respectively.

vortices comes from the work done by the relative movement of a body through a fluid, less work is done when the vortex street is weaker and hence the drag is lower. Therefore, the degree of drag reduction achieved with the current forcing methodology is in line with the significant attenuation of the vortex shedding strength.

Figure 27 plots  $\langle c_d \rangle / \langle c_{d,0} \rangle$  alongside  $|\widehat{\Gamma}_x|$  of the von Kármán vortex loops as the blue solid lines. As in figure 25, plotting  $\langle c_d \rangle / \langle c_{d,0} \rangle$  as a function of  $(R^2/St_j)^{0.5}$  provides a much better collapse between the two  $Re_d$  cases than would be achieved with  $R$  or  $C_\mu$ . This provides further evidence that the effectiveness of the current forcing methodology is more closely related to the wall-normal penetration distance of the jet near the trailing edge rather than the emitted jet strength. The maximum net drag reduction for both  $Re_d$  occurs at around  $(R^2/St_j)^{0.5} \approx 2.5-3$ , which also corresponds to when  $|\widehat{\Gamma}_x|$  is maximised. In agreement with the observations of Rodriguez (1991), this correspondence supports the hypothesis that the drag reduction is proportional to the amount of spanwise vorticity realigned into streamwise vorticity. By extension, it also suggests that similar results can be achieved with this forcing scheme for other bluff-body geometries that feature vortex shedding, and can be used to provide guidance in future studies to design better actuators or forcing strategies.

#### 4. Conclusion

Distributed forcing from an array of synthetic jet actuators on a profiled BTE body was experimentally investigated at  $Re_d = 2500$  and  $5000$ . Each of the synthetic jets in the array induced an upwash of fluid near their centreline planes and a downwash of fluid closer to the slot edge planes, forming pairs of streamwise vortices. As a result, the thickness of the separated shear layers varied along the span and spanwise vorticity in the shear layers tilted into streamwise vortices.

The forcing amplitude controlled the extent to which the vortical structures generated by the jets penetrated in the cross-flow. When  $\{Re_d = 2500, R = 3.1\}$  and  $\{Re_d = 5000, R = 1.9\}$ , the jets penetrated approximately up the edges of the boundary layers, generating

strong streamwise vortices inside the separated shear layers. This provided the most effective perturbations to the wake at those  $Re_d$ , attenuating the vortex shedding and reducing the velocity fluctuations in the wake. For the  $\{Re_d = 2500, R = 3.1\}$  case in particular, the wake width was found to decrease across the entire span and the spanwise circulation of the von Kármán vortices was reduced by about 35% compared to the unforced case. Forcing at higher amplitudes at those  $Re_d$  resulted in the jet vortical structures extending outside of the boundary layers, increasing the width of the wake near the jet centreline planes and worsening the overall drag reduction. Therefore, there is a critical forcing amplitude which corresponds to when the jets penetrate up to the edges of the boundary layers and provides roughly the greatest drag reduction.

Due to forcing, the vortex shedding exhibited three-dimensionality consistent with the spanwise variations in the separated shear layers. Most importantly, the attenuation of the vortex shedding by forcing was accompanied by the emergence of counter-rotating streamwise vortex pairs on both sides of the wake in a  $\{y, z\}$  cross-plane at  $x = 4d$ , which was well downstream of the von Kármán vortex formation length. The spanwise distance between positive and negative streamwise vortices was approximately  $1.2d$ , and the pattern repeated along the span with a wavelength of  $2.4d$ , matching the spacing of the actuators. In all cases the vortex shedding frequency,  $\widehat{St}_v$ , did not vary along the span, indicating that the current distributed forcing strategy produces an organised wake structure. A constant  $\widehat{St}_v$  along the span is in accordance with some previous studies of distributed forcing, such as the tab-based perturbations of Park *et al.* (2006) and cylinder waviness of Lam *et al.* (2004), but is in contrast to other studies, such as Tombazis & Bearman (1997), Bearman & Owen (1998), Bhattacharya & Gregory (2018) and Ling & Zhao (2009). It was argued that the reason for the different wake structures in these studies is that the present forcing wavelength of  $\lambda_z = 2.4d$  is in a low-wavelength regime.

The measurements in the cross-planes of the wake were phase-averaged with respect to the shedding cycle to reveal the three-dimensional structure of the forced wake. Over a shedding cycle, the magnitude of streamwise vorticity concentrations varied periodically and the streamwise vortices alternated between both sides of the wake. This vortical symmetry is similar to that reported by Park *et al.* (2006) and Zhang & Lee (2005) for different passive three-dimensional perturbations in the low-wavelength regime. An approximation of the vortex shedding structure in three dimensions was obtained by stacking the phase-averaged two-dimensional planar measurements at  $x = 4d$ , which showed that the streamwise vortices are essentially loops that are pulled out of the cores of the von Kármán vortices. The loops exist in the braid region of the wake and link successive cycles of shed vortices. Therefore, the attenuation of the von Kármán vortices by forcing is interpreted as being due to the tilting of the principally spanwise von Kármán vortices into the streamwise direction. Because the vortex street has anti-symmetry and the streamwise vortices in the wake emerge from this structure, the streamwise vortices rotate in opposite directions in the  $y < 0$  and  $y > 0$  halves of the wake at a given  $z$  location. This explains why the sense of rotation of a streamwise vortex at a given  $z$  location appears to switch once per shedding cycle. The vortical symmetry of the forced wake is similar to that exhibited by the mode A secondary instability (Williamson 1996); however, the mode A has a spanwise wavelength of  $\approx 4d$  and occurs in the wake transition regime, not the turbulent wake regime of the present study. In contrast, the mode B secondary instability may exist at the  $Re_d$  range of the present investigation, but its spanwise wavelength is  $\approx 1d$  and its vortical symmetry is completely different. This indicates that the vortex street can be significantly realigned by distributed forcing without matching the wavelength to a secondary instability.

The relationship between the drag reduction and the concentration of streamwise vortices in the wake was investigated by testing a range of forcing amplitudes. An alternative scaling for the forcing amplitude was proposed as  $(R^2/St_j)^{0.5}$  which is based on the jet penetration distance. It was found to better collapse the present results between the different  $Re_d$  than  $R$  or  $C_\mu$ . This indicates that the generation of streamwise vorticity with the present methodology is more closely related to how the jets penetrate in the flow rather than from momentum considerations. An implication of this is that if  $Re_d$  is controlled through  $u_\infty$ , as it is in the present study, then the maximum potential of the synthetic jet array to control the wake is reduced when  $Re_d$  increases because the boundary layers become thinner. However, provided that the forcing amplitude is low enough that the jets do not penetrate beyond the boundary layer edges, the relative effectiveness of the forcing may be expected to be better for the same  $R$  at higher  $Re_d$  because of the change in boundary layer thickness. In line with the hypothesis, a clear trend of decreasing drag with stronger streamwise vortices was exhibited up to the critical forcing amplitudes at  $Re_d = 2500$  and  $5000$ . This implies that many different types of three-dimensional perturbations should be able to attenuate the vortex street for various bluff-body geometries, and that the major factor controlling the effectiveness of these types of strategies is how well the perturbations tilt spanwise vorticity into streamwise vorticity.

**Funding.** Financial support for this research was provided by Natural Sciences and Engineering Research Council of Canada (NSERC) Discovery Grants (RGPIN-2014-03798 and RGPIN-2019-07108) and the Percy Edward Hart Professorship in Aerospace Engineering. The first author would also like to acknowledge a scholarship from NSERC and an Ontario Graduate scholarship.

**Declaration of interests.** The authors report no conflict of interest.

### Appendix A. Phase-averaging vortex shedding directly from the velocity field

The POD phase-averaging methodology outlined by van Oudheusden *et al.* (2005) requires streamwise spatial information in order to work. Therefore, it is not possible to apply the POD methodology to phase-average measurements in the  $\{y, z\}$  cross-plane. Instead, the velocity variations at a point near the outer edge of the von Kármán vortices close to the free stream are relied upon. At such a point, the turbulent velocity fluctuations are not very large and the  $u$  and  $v$  components are periodically modulated by the passage of the von Kármán vortices. For example, the phase-averaged variation of  $\tilde{u}$  and  $\tilde{v}$  from the streamwise plane at  $Re_d = 2500$  and without forcing at  $\{x, y\} = \{4d, 1.25d\}$  is plotted in figure 28. It is clear that  $\tilde{u}$  and  $\tilde{v}$  vary sinusoidally at this location in the wake and, in particular, that  $\tilde{u}$  leads  $\tilde{v}$  by  $90^\circ$ . This relationship should hold for the instantaneous  $u$  and  $v$  fluctuations in the velocity field, except that instantaneously there are also competing random fluctuations.

In the cross-plane, vortex shedding phase information for the instantaneous snapshots can be obtained by analysing the relationship between  $u$  and  $v$  at a similar location in the wake. Because the cross-plane has spanwise information, the  $u$  and  $v$  signals are averaged along the span to help filter out turbulent fluctuations. A disadvantage of spanwise averaging is that random large-scale spanwise variations in the vortex shedding are not resolved. Therefore, this approach is best applied over spanwise distances less than the streamwise wavelength of the vortex shedding. The notation adopted here uses  $\langle \cdot \rangle$  to indicate a spanwise average. In the cross-plane, the relationship between

$$\mathcal{U}(t) = \langle u(y_p, t) \rangle \quad \text{and} \quad \mathcal{V}(t) = \langle v(y_p, t) \rangle \quad (\text{A1})$$

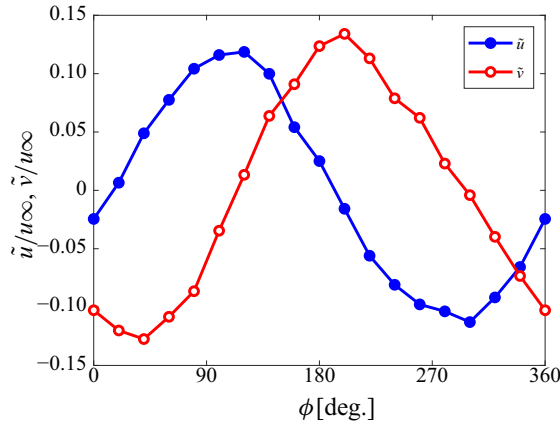


Figure 28. Variation of  $\tilde{u}$  and  $\tilde{v}$  over the vortex shedding cycle at  $\{x = 4d, y = 1.25d\}$  from the streamwise plane when  $Re_d = 2500$ . The phase average was performed using a POD methodology. Note that the time-averaged mean is removed.

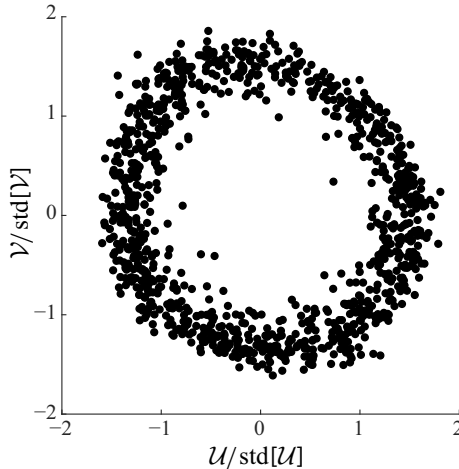


Figure 29. Scatter plot of the instantaneous variations of  $\mathcal{U}(t)$  and  $\mathcal{V}(t)$  at  $\{x, y\} = \{4d, 1.25d\}$  and spanwise-averaged in the range  $-1.6d \leq z \leq 1.6d$  for the  $Re_d = 2500$  case with no forcing.

is considered, where  $y_p$  is a given  $y$  location and the spanwise averages are evaluated in the range  $-1.6d \leq z \leq 1.6d$ .

The instantaneous variations of  $\mathcal{U}$  and  $\mathcal{V}$  are plotted against each other for the  $\{Re_d = 2500, R = 0\}$  case with  $y_p = 1.25d$  in figure 29. The axes are normalised by the respective standard deviations to scale the amplitude of the fluctuations. There is a clear relationship between  $\mathcal{U}$  and  $\mathcal{V}$  that traces out a circle.

It was found that  $y_p = 1.05d$  and  $y_p = 1.25d$  were good locations to obtain phase references for the  $x = 1d$  and  $x = 4d$  PIV cross-planes, respectively. They are close enough to the wake centreline that the coherent fluctuations are sufficiently strong to be picked up, but far enough away that the fluctuations are not obscured by turbulence. These locations are also well positioned because they are outside of the part of the wake with the greatest spanwise variations in the forcing cases that the jets do not significantly penetrate outside of the boundary layers. Note that the  $y_p$  location selected for the  $x = 4d$  plane is slightly

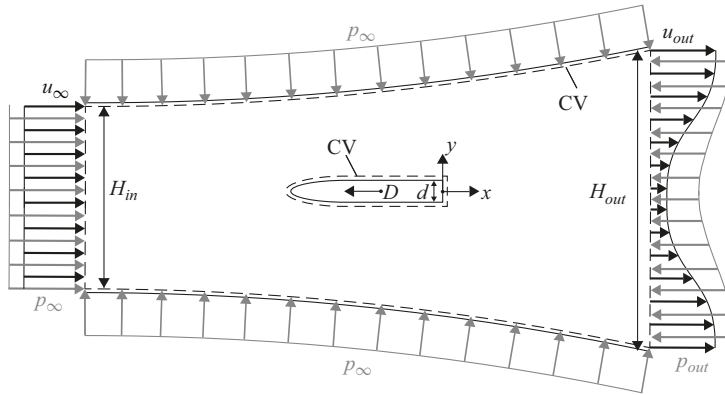


Figure 30. Planar control volume of the body in a wind tunnel, showing the velocity flow and pressure forces.

farther away from the centreline than for the  $x = 4d$  plane to compensate for the von Kármán vortices diffusing downstream. For the relatively higher-forcing-amplitude cases where the jets extend well outside the boundary layers, obtaining the vortex shedding phase reference with this procedure is less valid because the jets introduce significant velocity fluctuations even in the outer regions of the wake which are not associated with vortex shedding (especially in the  $x = 1d$  plane). Hence, none of the high-forcing-amplitude cases are phase-averaged with this procedure in the paper. In the unforced and relatively lower-forcing-amplitude cases, phase references similar to those calculated from the selected coordinates can also be obtained within the range  $0.75d < y_p < 1.75d$ ; however, the relationship between  $\mathcal{U}$  and  $\mathcal{V}$  starts to deviate away from circular towards the ends of those  $y_p$  extremes.

The symmetry of vortex shedding across the wake centreline is  $\tilde{u}(x, y) = -\tilde{u}(x, -y)$  and  $\tilde{v}(x, y) = \tilde{v}(x, -y)$ . This symmetry is exploited to improve the phase calculations by taking into account both sides of the wake. Therefore, the signals that are used to create the phase reference are

$$\begin{aligned} \mathcal{U}^*(t) &= \langle u(y_p, t) - u(-y_p, t) \rangle, \\ \mathcal{V}^*(t) &= \langle v(y_p, t) + v(-y_p, t) \rangle, \end{aligned} \quad (\text{A2})$$

spanwise-averaged over  $-1.6d \leq z \leq 1.6d$ , and the shedding phase is calculated as

$$\phi_v(t) = \arctan \frac{\mathcal{V}^*(t)/\text{std}[\mathcal{V}^*(t)]}{\mathcal{U}^*(t)/\text{std}[\mathcal{U}^*(t)]}. \quad (\text{A3})$$

## Appendix B. Drag from planar momentum balance

The drag force can be computed through a streamwise momentum balance over a control volume large enough to encompass the body and the surrounding incompressible flow:

$$\sum F_x = \rho \iint_S \mathbf{V}(\mathbf{V} \cdot \mathbf{n}) dS, \quad (\text{B1})$$

where  $\mathbf{n} = n_x \mathbf{i} + n_y \mathbf{j} + n_z \mathbf{k}$  is the normal vector to the control volume. The control volume shown in figure 30 is expanding to account for the deflection of the streamlines by the body such that the flow enters and exits the control volume only along the  $\{y, z\}$  plane boundaries.

The flow is assumed to be uniform and steady at the inflow plane of the control volume, which has a height of  $H_{in}$ . Assuming that the only external force that acts on the control volume is the drag,  $D$ , in the  $x$  direction, the Reynolds-averaged  $x$  momentum equation evaluates as

$$\begin{aligned}
 & -D + \int_{S,in} p_{\infty} n_x \ell_z dy - \int_{S,out} p n_x \ell_z dy \\
 & = \rho \ell_z \int_{S,out} (\bar{u}^2 + \overline{u'u'}) dy - \rho \ell_z H_{in} u_{\infty}^2 + \iint_S (\tau_{xx} n_x + \tau_{xy} n_y + \tau_{xz} n_z) dS, \quad (B2)
 \end{aligned}$$

where  $p$  is the pressure,  $\infty$  represents a condition in the free stream and  $\ell_z$  is the thickness of the control volume along  $z$ . The  $u_{\infty}^2$  and  $\bar{u}^2$  terms represents the momentum from the mean flow, and the difference between them is typically the main contributor to the overall momentum deficit. The  $\overline{u'u'}$  term is the Reynolds stress term, which accounts for the momentum carried by the streamwise velocity fluctuations. According to Antonia & Rajagopalan (1990), the Reynolds stress term is an important contributor to the calculated drag up to  $x \approx 30d$  for cylinders at  $Re_d = 5600$ . The viscous stresses are represented as  $\tau_{xx}$ ,  $\tau_{xy}$ ,  $\tau_{xz}$ , but are neglected because they are significantly smaller ( $< 1\%$ ) than the other components for flows such as the present case above the wake transition regime. Equation (B2) can be rearranged for  $D$  as

$$D = \int_S (p_{\infty} - p_{out}(y)) n_x \ell_z dy + \rho \ell_z H_{in} u_{\infty}^2 - \rho \ell_z \int_{S,out} \bar{u}^2 dy - \rho \ell_z \int_{S,out} \overline{u'u'} dy. \quad (B3)$$

The pressure variation in the wake can be approximated based on the momentum equation for shear layers (Townsend 1956):

$$\frac{1}{\rho} \frac{\partial p}{\partial y} = -\frac{\partial \overline{v'v'}}{\partial y}, \quad (B4)$$

which can be integrated along  $y$  for the outflow plane from a point in the free stream where  $\overline{v'v'} \approx 0$  to a point in the wake to obtain

$$p(y) = p_{\infty,out} - \rho \overline{v'v'}(y). \quad (B5)$$

Assuming that the pressure in the free stream at the outflow plane is the same as at the inflow plane,  $p_{\infty,out} = p_{\infty}$ , (B5) can be substituted into (B3) to obtain

$$D = \rho \ell_z H_{in} u_{\infty}^2 - \rho \ell_z \int_{S,out} \bar{u}^2 dy - \rho \ell_z \int_{S,out} \overline{u'u'} dy + \rho \ell_z \int_{S,out} \overline{v'v'} dy. \quad (B6)$$

Continuity of the mass flow rate ( $\dot{m}$ ) is used to find the height of the inflow plane as

$$\begin{aligned}
 \dot{m}_{in} & = \dot{m}_{out}, \\
 \rho \ell_z H_{in} u_{\infty} & = \rho \ell_z \int_{S,out} (\bar{u}^2 + \bar{v}^2 + \bar{w}^2)^{1/2} dy, \quad (B7)
 \end{aligned}$$

considering the total outgoing velocity. Symmetry of the wake about  $y = 0$  means that the net contribution of  $\bar{v}$  to the mass flux can be neglected. From this it follows that

$$H_{in} = \frac{\int_{S,out} (\bar{u}^2 + \bar{w}^2)^{1/2} dy}{u_{\infty}}, \quad (B8)$$

which can be substituted into (B6) and normalised appropriately so that the drag coefficient for a cross-sectional plane is

$$c_d = \frac{D}{\frac{1}{2}\rho\ell_z du_\infty^2} = \frac{2}{u_\infty^2} \int_{S,out} \left( u_\infty (\bar{u}^2 + \bar{w}^2)^{1/2} - \bar{u}^2 - \overline{u'u'} + \overline{v'v'} \right) d\left(\frac{y}{d}\right). \quad (\text{B9})$$

#### REFERENCES

- AHMED, A. & BAYS-MUCHMORE, B. 1992 Transverse flow over a wavy cylinder. *Phys. Fluids* **4** (9), 1959–1967.
- AHMED, A., KHAN, M.J. & BAYS-MUCHMORE, B. 1993 Experimental investigation of a three-dimensional bluff-body wake. *AIAA J.* **31** (3), 559–563.
- ANTONIA, R.A. & RAJAGOPALAN, S. 1990 Determination of drag of a circular cylinder. *AIAA J.* **28** (10), 1833–1834.
- ASHURST, W.T. & MEIBURG, E. 1988 Three-dimensional shear layers via vortex dynamics. *J. Fluid Mech.* **189**, 87–116.
- BEARMAN, P.W. 1965 Investigation of the flow behind a two-dimensional model with a blunt trailing edge and fitted with splitter plates. *J. Fluid Mech.* **21** (2), 241–255.
- BEARMAN, P.W. & OWEN, J.C. 1998 Reduction of bluff-body drag and suppression of vortex shedding by the introduction of wavy separation lines. *J. Fluids Struct.* **12** (1), 123–130.
- BERK, T. & GANAPATHISUBRAMANI, B. 2019 Effects of vortex-induced velocity on the development of a synthetic jet issuing into a turbulent boundary layer. *J. Fluid Mech.* **870**, 651–679.
- BERK, T., HUTCHINS, N., MARUSIC, I. & GANAPATHISUBRAMANI, B. 2018 Trajectory of a synthetic jet issuing into high-Reynolds-number turbulent boundary layers. *J. Fluid Mech.* **856**, 531–551.
- BHATTACHARYA, S. & GREGORY, J.W. 2015 Investigation of the cylinder wake under spanwise periodic forcing with a segmented plasma actuator. *Phys. Fluids* **27** (1), 014102.
- BHATTACHARYA, S. & GREGORY, J.W. 2018 Optimum-wavelength forcing of a bluff body wake. *Phys. Fluids* **30** (1), 015101.
- BREDE, M., ECKELMANN, H. & ROCKWELL, D. 1996 On secondary vortices in the cylinder wake. *Phys. Fluids* **8** (8), 2117–2124.
- CAI, J., CHNG, T.L. & TSAI, H.M. 2008 On vortical flows shedding from a bluff body with a wavy trailing edge. *Phys. Fluids* **20** (6), 064102.
- CANTWELL, B. & COLES, D. 1983 An experimental study of entrainment and transport in the turbulent near wake of a circular cylinder. *J. Fluid Mech.* **136**, 321–374.
- CUI, G.P., FENG, L.H. & LIU, L.Y. 2020 Spanwise modulation of a three-dimensional wake using distributed forcing. *Aerosp. Sci. Technol.* **104**, 105934.
- DAREKAR, R.M. & SHERWIN, S.J. 2001 Flow past a square-section cylinder with a wavy stagnation face. *J. Fluid Mech.* **426**, 263–295.
- DOBRE, A., HANGAN, H. & VICKERY, B.J. 2006 Wake control based on spanwise sinusoidal perturbations. *AIAA J.* **44** (3), 485–492.
- EFRON, B. 1979 Bootstrap methods: another look at the jackknife. *Ann. Statist.* **7** (1), 1–26.
- EROGLU, A. & BREIDENTHAL, R. 2001 Structure, penetration and mixing of pulsed jets in crossflow. *AIAA J.* **39** (3), 417–423.
- FRIC, T.F. & ROSHKO, A. 1994 Vortical structure in the wake of a transverse jet. *J. Fluid Mech.* **279**, 1–47.
- GAI, S.L. & SHARMA, S.D. 1981 Experiments on the reduction of base drag of a blunt trailing edge aerofoil in subsonic flow. *Aero. J.* **85** (844), 206–210.
- GIBEAU, B., KOCH, C.R. & GHAEMI, S. 2018 Secondary instabilities in the wake of an elongated two-dimensional body with a blunt trailing edge. *J. Fluid Mech.* **846**, 578–604.
- GLEZER, A. 1988 The formation of vortex rings. *Phys. Fluids* **31** (12), 3532–3542.
- GLEZER, A. & AMITAY, M. 2002 Synthetic jets. *Ann. Rev. Fluid Mech.* **34** (1), 503–529.
- HULTMARK, M. & SMITS, A.J. 2010 Temperature corrections for constant temperature and constant current hot-wire anemometers. *Meas. Sci. Technol.* **21** (10), 105404.
- HUNT, J.C.R., WRAY, A.A. & MOIN, P. 1988 Eddies, streams, and convergence zones in turbulent flows, In 2. Proceedings of the 1988 Summer Program, pp. 193–208.
- HWANG, Y., KIM, J. & CHOI, H. 2013 Stabilization of absolute instability in spanwise wavy two-dimensional wakes. *J. Fluid Mech.* **727**, 346–378.
- JABBAL, M. & ZHONG, S. 2008 The near wall effect of synthetic jets in a boundary layer. *Intl J. Heat Fluid Flow* **29** (1), 119–130.
- KARAGOZIAN, A.R. 2014 The jet in crossflow. *Phys. Fluids* **26** (10), 101303.

- VON KÁRMÁN, T. 1912 Über den Mechanismus des Widerstands, den ein bewegter Körper in einer Flüssigkeit erfährt. *Göttingen Nachr. Math. Phys. Kl* 547–556.
- KIM, J. & CHOI, H. 2005 Distributed forcing of flow over a circular cylinder. *Phys. Fluids* 17 (3), 033103.
- KIM, J., HAHN, S., KIM, J., LEE, D., CHOI, J., JEON, W.-P. & CHOI, H. 2004 Active control of turbulent flow over a model vehicle for drag reduction. *J. Turbul* 5 (1), 019.
- LAM, K. & LIN, Y.F. 2008 Large eddy simulation of flow around wavy cylinders at a subcritical Reynolds number. *Intl J. Heat Fluid Flow* 29 (4), 1071–1088.
- LAM, K. & LIN, Y.F. 2009 Effects of wavelength and amplitude of a wavy cylinder in cross-flow at low Reynolds numbers. *J. Fluid Mech.* 620, 195–220.
- LAM, K., WANG, F.H., LI, J.Y. & SO, R.M.C. 2004 Experimental investigation of the mean and fluctuating forces of wavy (varicose) cylinders in a cross-flow. *J. Fluids Struct* 19 (3), 321–334.
- LASHERAS, J.C. & CHOI, H. 1988 Three-dimensional instability of a plane free shear layer: an experimental study of the formation and evolution of streamwise vortices. *J. Fluid Mech.* 189, 53–86.
- LASHERAS, J.C. & MEIBURG, E. 1990 Three-dimensional vorticity modes in the wake of a flat plate. *Phys. Fluids* 2 (3), 371–380.
- LEE, S.J. & NGUYEN, A.T. 2007 Experimental investigation on wake behind a wavy cylinder having sinusoidal cross-sectional area variation. *Fluid Dyn. Res.* 39 (4), 292–304.
- LI, Y., BAI, H. & GAO, N. 2015 Drag of a D-shaped bluff body under small amplitude harmonic actuation. *Theor. Appl. Mech. Lett.* 5 (1), 35–38.
- LING, G.C. & ZHAO, H.L. 2009 Vortex dislocations in wake-type flow induced by spanwise disturbances. *Phys. Fluids* 21 (7), 073604.
- MAHESH, K. 2013 The interaction of jets with crossflow. *Ann. Rev. Fluid Mech.* 45 (1), 379–407.
- MEIBURG, E. & LASHERAS, J.C. 1988 Experimental and numerical investigation of the three-dimensional transition in plane wakes. *J. Fluid Mech.* 190, 1–37.
- NAGHIB-LAHOUTI, A. & HANGAN, H. 2010 Active flow control for reduction of fluctuating aerodynamic forces of a blunt trailing edge profiled body. *Intl J. Heat Fluid Flow* 31 (6), 1096–1106.
- NAGHIB-LAHOUTI, A., HANGAN, H. & LAVOIE, P. 2015 Distributed forcing flow control in the wake of a blunt trailing edge profiled body using plasma actuators. *Phys. Fluids* 27 (3), 035110.
- NAGHIB-LAHOUTI, A., LAVOIE, P. & HANGAN, H. 2014 Wake instabilities of a blunt trailing edge profiled body at intermediate Reynolds numbers. *Exp. Fluids* 55 (7), 1779.
- PARK, H., LEE, D., JEON, W.P., HAHN, S., KIM, J., KIM, J. & CHOI, H. 2006 Drag reduction in flow over a two-dimensional bluff body with a blunt trailing edge using a new passive device. *J. Fluid Mech.* 563, 389–414.
- PETRUSMA, M.S. & GAI, S.L. 1996 Bluff body wakes with free, fixed, and discontinuous separation at low Reynolds numbers and low aspect ratio. *Exp. Fluids* 20 (3), 189–198.
- PONCET, P., HILDEBRAND, R., COTT, G.H. & KOUMOUTSAKOS, P. 2008 Spatially distributed control for optimal drag reduction of the flow past a circular cylinder. *J. Fluid Mech.* 599, 111–120.
- RATHNASINGHAM, R. & BREUER, K.S. 2003 Active control of turbulent boundary layers. *J. Fluid Mech.* 495 (11), 209–233.
- RODRIGUEZ, O. 1991 Base drag reduction by control of the three-dimensional unsteady vortical structures. *Exp. Fluids* 11 (4), 218–226.
- ROSHKO, A. 1954 On the drag and shedding frequency of two-dimensional bluff bodies. *NACA Tech. Note* 3169, 1–29.
- RYAN, K., THOMPSON, M.C. & HOURIGAN, K. 2005 Three dimensional transition in the wake of bluff elongated cylinders. *J. Fluid Mech.* 538, 1–29.
- SAU, R. & MAHESH, K. 2008 Dynamics and mixing of vortex rings in crossflow. *J. Fluid Mech.* 604, 389–409.
- SMITH, D. 2002 Interaction of a synthetic jet with a crossflow boundary layer. *AIAA J.* 40 (11), 2277–2288.
- TANNER, M. 1972 A method of reducing the base drag of wings with blunt trailing edges. *Aeronaut. Q* 23 (1), 15–23.
- TOMBAZIS, N. & BEARMAN, P.W. 1997 A study of three-dimensional aspects of vortex shedding from a bluff body with a mild geometric disturbance. *J. Fluid Mech.* 330 (85), 85–112.
- TOWNSEND, A. 1956 *The Structure of Turbulent Shear Flow*. Cambridge University Press.
- TRICOUROU, F.A., AMITAY, M. & VAN BUREN, T. 2023 A parametric study of rectangular jets issuing into a laminar crossflow. *Exp. Fluids* 64 (123), 15.
- VAN BUREN, T., BEYAR, M., LEONG, C.M. & AMITAY, M. 2016 Three-dimensional interaction of a finite-span synthetic jet in a crossflow. *Phys. Fluids* 28 (3), 037105.
- VAN BUREN, T., WHALEN, E. & AMITAY, M. 2014 Vortex formation of a finite-span synthetic jet: effect of rectangular orifice geometry. *J. Fluid Mech.* 745, 180–207.

- VAN OUDHEUSDEN, B.W., SCARANO, F., VAN HINSBERG, N.P. & WATT, D.W. 2005 Phase-resolved characterization of vortex shedding in the near wake of a square-section cylinder at incidence. *Exp. Fluids* **39** (1), 86–98.
- WILLIAMSON, C.H.K. 1992 The natural and forced formation of spot-like vortex dislocations in the transition of a wake. *J. Fluid Mech.* **243**, 393–441.
- WILLIAMSON, C.H.K. 1996 Three-dimensional wake transition. *J. Fluid Mech.* **328**, 345–407.
- YAVUZKURT, S. 1984 A guide to uncertainty analysis of hot-wire data. *J. Fluids Engng* **106** (2), 181–186.
- ZHANG, W. & LEE, S.J. 2005 PIV measurements of the near-wake behind a sinusoidal cylinder. *Exp. Fluids* **38** (6), 824–832.